MODELING CURE DEPTH DURING PHOTOPOLYMERIZATION OF MULTIFUNCTIONAL ACRYLATES

A Thesis
Presented to
The Academic Faculty

by

Aparna Boddapati

In Partial Fulfillment
of the Requirements for the Degree
Master of Science in the
School of Chemical & Biomolecular Engineering

Georgia Institute of Technology
May 2010

MODELING CURE DEPTH DURING PHOTOPOLYMERIZATION OF MULTIFUNCTIONAL ACRYLATES

Approved by:

Dr. Martha A. Grover, Advisor
School of Chemical & Biomolecular Engineering
Georgia Institute of Technology

Dr. Clifford Henderson, Advisor
School of Chemical & Biomolecular Engineering
Georgia Institute of Technology

Dr. Haskell Beckham
School of Polymer, Textile & Fiber Engineering
Georgia Institute of Technology

Date Approved: February 11, 2010

To my Mother,who has always put my needs above her own, and my Father, who taught me how to face uncertainty with courage.

ACKNOWLEDGEMENTS

I would like to thank my advisors Dr. Martha Grover, and Dr. Cliff Henderson for giving me the opportunity to work on this project. They guided me with patience, and provided insightful and challenging ideas. I am especially grateful that they worked together to give me unique direction, and shared their collective knowledge with me. I would also like to thank Dr. Breedveld for allowing me access to equipment in his lab, and giving feedback on experimental results. In addition, I am thankful for Dr. Rosen's support; his involvement gave me access to a great deal of information. I would also like to thank Dr. Beckham, for agreeing to be a part of my committee.

I am very thankful to Dr. Santosh Rahane, who did all the earlier characterization experiments, and also provided assistance when I was starting my own experimental work. I would also like to thank Dr. Ryan Slopek, the experimental data from his thesis was central to my conclusions.

Dr. Fei Ding and Amit Jariwala helped me to test different measurement techniques. They patiently assisted me as I tried different methods of measurements, and I will always be grateful for their assistance in collecting data for my Thesis.

I would like to thank CIBA Vision for funding my research work and providing such an interesting topic to work on.

I cannot begin to name all the wonderful people in our department that helped me with anything I needed, thank you for being there for me. I am very grateful for the help I received from my group members Jonathan and Andres, who helped me with proofreading and formatting problems. I also want to thank my parents, for encouraging me to push myself to the best of my abilities. I am grateful for the support I received from my sister, Deepti, who always lends me a sympathetic ear.

TABLE OF CONTENTS

LIST OF TABLES

LIST OF FIGURES

SUMMARY

The photopolymerization of multifunctional acrylates leads to the formation of a complex and insoluble network due to cross-linking. This characteristic is a useful property for stereolithography applications, where solid parts of the desired shape are cured using a pre-determined energy exposure profile. Traditionally, the required energy exposure is determined using a critical energy–depth of penetration, or E_c–D_p, model. The parameters E_c and D_p, are usually fit to experimental data at a specific resin composition and cure intensity. As a result, since the E_c–D_p model does not explicitly incorporate cure kinetics, it cannot be used for a different set of process conditions without first obtaining experimental data at the new conditions. Thus, the E_c–D_p model does not provide any insight when a new process needs to be developed, and the best processing conditions are unknown.

The kinetic model for multifunctional acrylate photopolymerization presented here is based on a set of ordinary differential equations (ODE), which can be used to predict part height versus exposure condition across varying resin compositions. Kinetic parameter information used in the model is obtained by fitting the model to double bond conversion data from Fourier Transform Infrared Spectroscopy (FTIR) measurements. An additional parameter, the critical conversion value, is necessary for determining the formation of a solid part of the desired height. The initial rate of initiation, R_i, combines all the factors that impact part height, and therefore, it is an important quantity that is required in order to find the critical conversion value. The critical conversion value is estimated using the R_i and T_{gel} value from microrheology measurements.

Information about network connectivity, which can be used to get properties such

as molecular weight, cannot be derived from models using traditional mass-action kinetics for the cross-linking system. Therefore, in addition to modeling the reaction using the ODE based model, the results from a statistical model based on Kinetic Monte Carlo (KMC) principles are also shown here. The KMC model is applicable in situations where the impact of chain length on the kinetics or molecular weight evolution is of interest. For the present project, the detailed information from network connectivity was not required to make part height predictions, and the conversion information from the ODE model was sufficient.

The final results show that the kinetic ODE model presented here, based on the critical conversion value, captures the impact of process parameters such as initiator concentration, light intensity, and exposure time, on the final part height of the object. In addition, for the case of blanket cure samples, the part height predictions from the ODE model make comparable predictions to the E_c–D_p model. Thus, the ODE model presented here is a versatile tool that can be used to determine optimum operating conditions during process development.

CHAPTER I

INTRODUCTION

1.1 Photopolymerization of multifunctional acrylates

The photopolymerization kinetics of multifunctional acrylates have been studied extensively since these polymers are used in a wide range of applications from lithography and coatings, to biologically related uses such as dental composites and contact lenses [3]. The vinyl bonds on acrylates react readily in the presence of radicals, and in the case of multifunctional acrylates, which have multiple vinyl groups per monomer, reactions between distinct chains are also possible. These types of reactions, known as cross-linking, bind different polymer chains in the reaction volume into an insoluble network. Several hydrogels that are used in tissue engineering are non-toxic derivatives of acrylates, and the cross-linking abilities of multifunctional acrylates are often exploited in these scenarios [9, 23].

Cross-linking does not take place in photopolymerization of monofunctional monomers, as shown in Figure 1. Since all the chains formed will be linear, the resulting polymer network is soluble. In contrast, the cross-linked networks formed by multifunctional monomers are insoluble. This durability is a desirable property in stereolithography applications, where polymer parts of various shapes are prepared using a computer generated exposure profile [17, 27, 32]. In photopolymerization, radicals are generated from the initiator when they receive energy from UV light. Based on the desired shape of the final object, the energy delivered to each area of the resin vat can be controlled to cure to the exact depth. By understanding the kinetics of polymerization, the cured shape and properties can be controlled more accurately. In addition, statistical methods of simulating the reaction sequence, such as the Monte

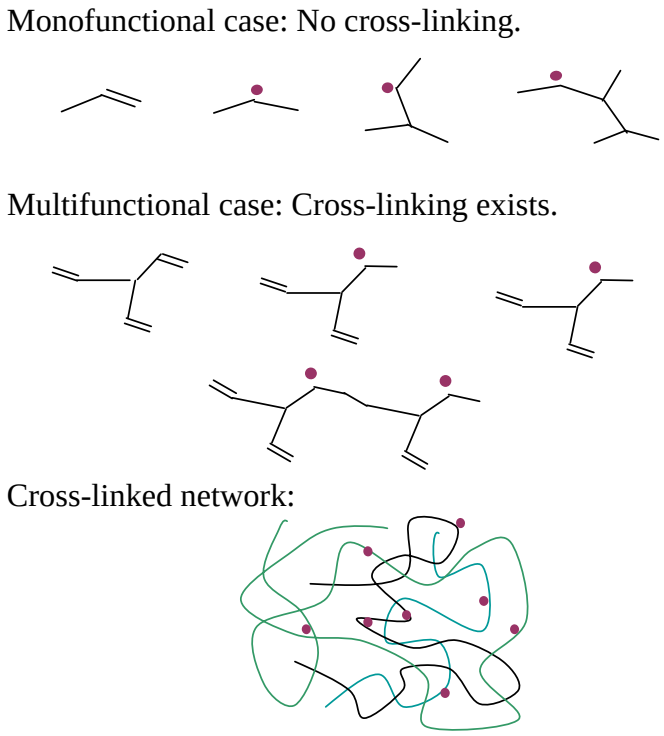

Figure 1: Simplified schematic of acrylate crosslinking.

Carlo method, can be used along with experimental methods to improve understanding of the photopolymerization reactions. Figure 4 contains an outline of how we developed the model and associated parameters.

1.2 Scope of this project

The exposure profiles used in stereolithography are typically generated using the relationship between the critical energy dose (E_c) and the associated cured part height (D_p) for a specific resin composition. This exposure profile is fed to a digital micromirror device (DMD) which can be used along with UV light to cure the pre-polymer resin, as shown in Figure 2. A DMD is an array of microscopic mirrors that can be turned ON or OFF individually. If the desired part requires high precision, the accurate determination of the critical energy required for cure becomes important. Traditional E_c–D_p models are designed to make predictions for a specific resin composition, since they do not explicitly incorporate the cure kinetics. Presented in the

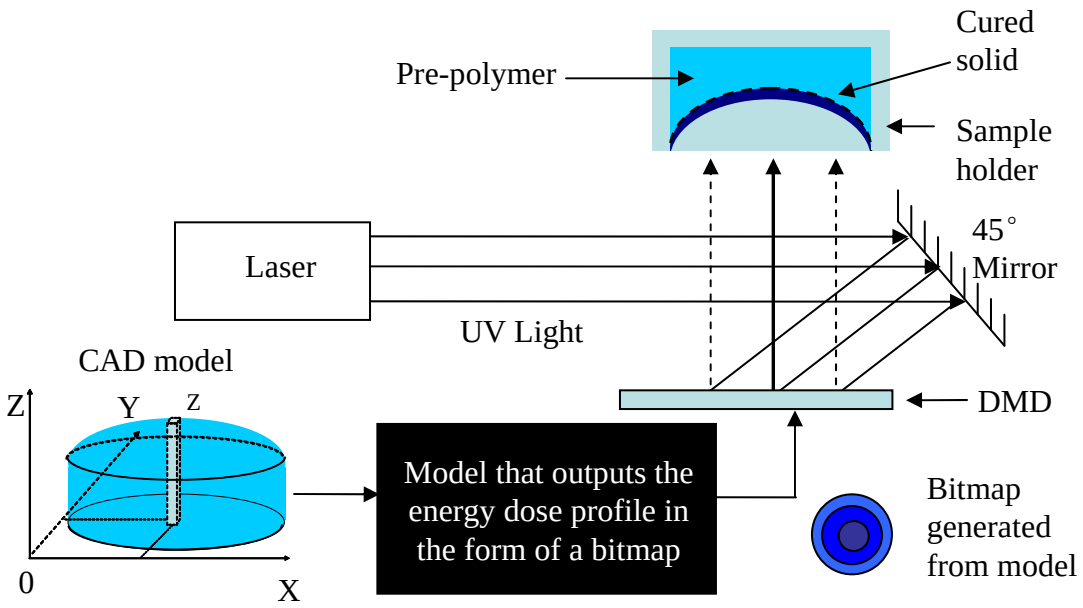

Figure 2: Simplified schematic of a stereolithography system. Typically, the digital micro-mirror device (DMD) receives the exposure profile from a bitmap representation of a computer aided design (CAD) model. The sample holder shown here has a curved bottom, which means that the part formed on top of this surface will retain that curvature.

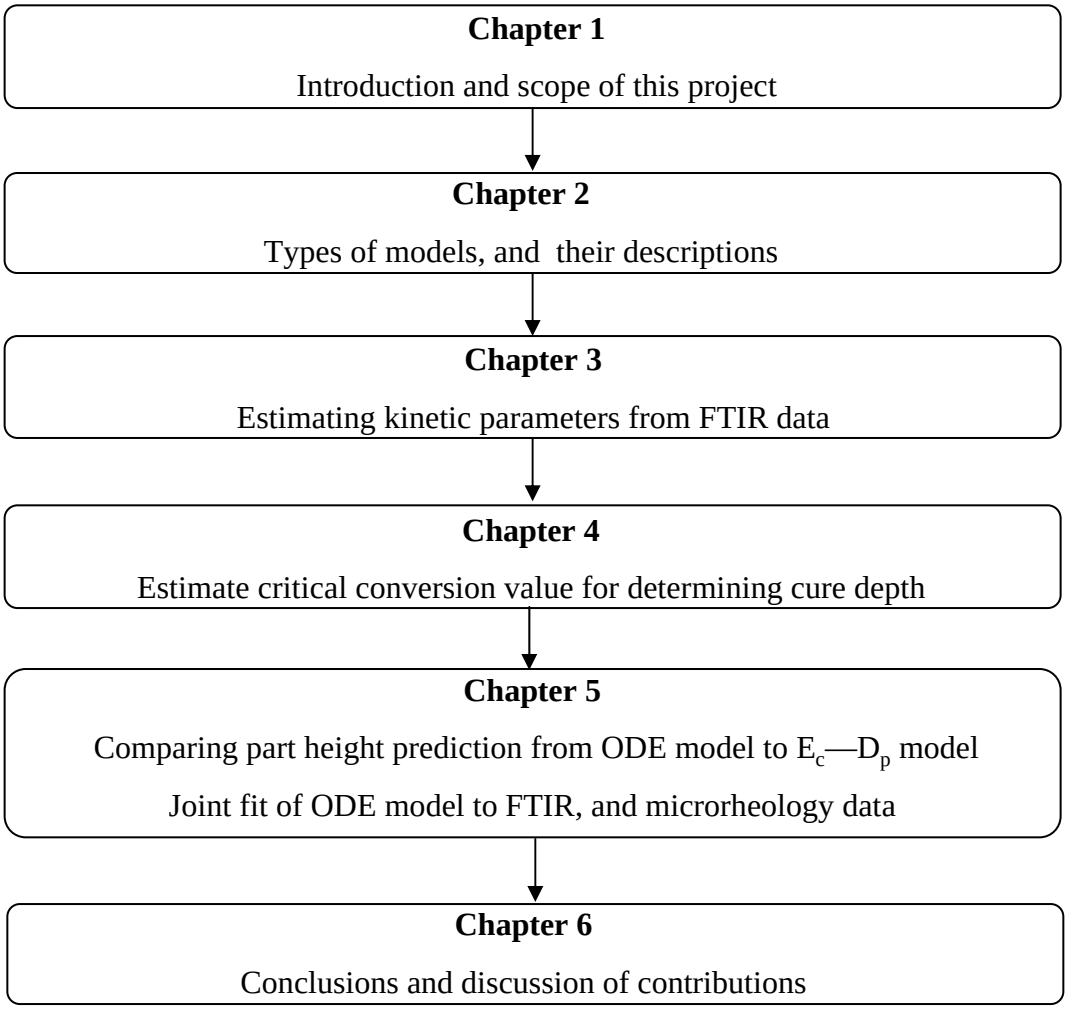

Figure 3: Outline of the chapters in the thesis

following chapters is a versatile model that is adaptable to changes in resin composition and is capable of representing the reactions occurring in the system.

Figure 3 contains a chapter outline. Chapter 2 describes models that are typically applied to predict polymerization reactions, and it also contains a description of the models used here. Chapter 3 shows all the Fourier Transform Infrared Spectroscopy (FTIR) experimental data, as well as the rate constants estimated from fitting to this data. In Chapter 4, the degree of cure necessary for making a solid part is obtained from fitting to the gel time data from microrheology. Finally, in Chapter 5, part height predictions from the ODE model are compared to an E_c–D_p model. The

versatile model presented in this thesis is capable of predicting cure height at various resin compositions, intensity levels and other initial conditions, because it includes cure kinetics.

CHAPTER II

MODELS FOR PREDICTING POLYMERIZATION

The typical reactants in a photopolymerization reaction are initiator molecules, In, free radicals generated by initiators, $R\bullet$, polymer chains, P, monomers, M, oxygen, O_2, and solvent. The dynamic concentration of each of these species can be described through a mathematical model based on the reaction mechanism. The reaction mechanism shown in Equations (1)–(10) is used in most photopolymerization simulations. Some models do not distinguish between a live chain, $P\bullet$, and a primary radical, $R\bullet$, in which case the sum of $R\bullet$ and $P\bullet$ equals the total number of active radicals or active sites. The first step is a decomposition event where an initiator molecule is decomposed to generate two radicals.

$$In \overset{k_d}{\rightarrow} 2R\bullet \tag{1}$$

Then, the radical is free to react with a monomer, thus initiating a polymer chain.

$$R\bullet + M \overset{k_p}{\rightarrow} P\bullet \tag{2}$$

Polymer chains propagate via reactions with available vinyl bonds that are on monomers, or on other polymer chains. When a reaction with vinyl bonds on polymer chains occurs, as in the case of multifunctional acrylates, the polymer becomes bigger.

$$P\bullet + M \overset{k_p}{\rightarrow} P\bullet \tag{3}$$

$$P\bullet + R\bullet \overset{k_p}{\rightarrow} P\bullet\bullet \tag{4}$$

$$P\bullet + P\bullet \overset{k_p}{\rightarrow} P\bullet\bullet \tag{5}$$

The reactive radical centers on polymer molecules, as well as live radicals, are terminated by reacting either with a free radical or a radical that is on a chain to make dead

polymer chains, P_{dead} and dead radicals, R_{dead}. Termination can occur either through combination or through disproportionation, and often both mechanisms are present for a given acrylate [3]. In the case of vinyl monomers, which include acrylates, it has been found that termination occurs mostly via combination [22]. Other possible effects are chain transfer to monomer and polymer, and molecular weight dependent termination caused by steric hindrance effects in propagation and termination events [19].

$$R\bullet + R\bullet \overset{k_t}{\rightarrow} 2R_{dead} \tag{6}$$

$$P\bullet + P\bullet \overset{k_t}{\rightarrow} P_{dead} \tag{7}$$

$$P\bullet + R\bullet \overset{k_t}{\rightarrow} P_{dead} \tag{8}$$

In addition to the propagation and termination reactions, oxygen in the reaction volume acts as a radical scavenger, and inhibits the propagation and termination reactions.

$$R\bullet + O_2 \overset{k_{toxy}}{\rightarrow} R_{dead} \tag{9}$$

$$P\bullet + O_2 \overset{k_{toxy}}{\rightarrow} P_{dead} \tag{10}$$

Equations (1)–(10) contain the typical reactions that take place in photopolymerization systems. These reactions can be simulated through models for photopolymerization, which can be divided into three categories: (A) non-connectivity based continuous models, such as a set of ordinary differential equations, (B) stochastic and discrete models that track the spatial location of all reactants, and (C) stochastic and discrete models that are non-spatial. The model selection will depend on the type of output information desired.

2.1 Continuous Models

In the case of monofunctional acrylates, the dynamic concentration of all the species in a well mixed bulk reaction volume can be defined by a set of ordinary differential

equations (ODEs) such as the ones shown in Equations (11)–(16).

$$\frac{d[In]}{dt} = -k_d[In] \tag{11}$$

$$\frac{d[R\bullet]}{dt} = 2k_d[In] - k_p[M][R\bullet] - 2k_t[P\bullet][R\bullet] - 2k_t[R\bullet]^2 - k_{toxy}[O_2][R\bullet] \tag{12}$$

$$\frac{d[M]}{dt} = -k_p[M][R\bullet] - k_p[M][P\bullet] \tag{13}$$

$$\frac{d[P\bullet]}{dt} = k_p[M][R\bullet] - 2k_t[P\bullet]^2 - 2k_t[P\bullet][R\bullet] - k_{toxy}[O_2][P\bullet] \tag{14}$$

$$\frac{d[P_{dead}]}{dt} = k_t[P\bullet]^2 + 2k_t[P\bullet][R\bullet] + k_{toxy}[O_2][P\bullet] \tag{15}$$

$$\frac{d[O_2]}{dt} = -k_{toxy}[O_2][R\bullet] - k_{toxy}[O_2][P\bullet] \tag{16}$$

Since all resulting polymer chains from monoacrylates will be linear, there will be no effects such as cross-linking that need to be accounted for. A model based on these equations can still be used to track the double bond conversion, radical concentration and oxygen concentration in multifunctional acrylate systems. However, the cross-linking property shown in Figure 1 of the multifunctional groups is not represented. The lack of network connectivity information in this model indicates that the concentration of polymer chains, dead or alive, $P\bullet$ or P_{dead}, cannot be computed. Additionally, in the case of multifunctional monomers, although the number of double bonds that have reacted can be tracked, the number of monomers that have polymerized cannot be computed. This type of connectivity information is once again necessary to compute the molecular weight of the gel in a multifunctional system. Other network details such as the location of a monomer or polymer chain, are also not modeled by traditional mass action kinetics in either mono- or multifunctional acrylates. Despite these limitations, the solutions to the ODEs in Equations (11)–(16) are used here to estimate rate constants in a multifunctional system, by comparing to experimental measurements for the earlier stages of reaction.

The rate of initiator decomposition for photopolymerization depends on the concentration of the initiator, the intensity of the light source, and the depth into the

absorbing medium [25]. Using the Beer Lambert law, the rate of initiator decomposition as a function of depth, z, into the sample has been developed [25]:

$$I'_{abs} = I_0 - I_0 e^{(-2.3\epsilon[In]z)} \tag{17}$$

$$I_{abs} = \frac{dI'_{abs}}{dz} = 2.3\epsilon[In]I_0 e^{(-2.3\epsilon[In]z)} \tag{18}$$

$$R_d = \phi I_{abs}\left(\frac{\lambda}{N_A\, h\, c}\right) = \phi\left(2.3\epsilon[In]I_0 e^{(-2.3\epsilon[In]z)}\right)\left(\frac{\lambda}{N_A\, h\, c}\right) \tag{19}$$

A combined rate constant term k_d, can then be described as follows:

$$k_d = 2.3\phi\epsilon I_0 e^{(-2.3\epsilon[In]z)}\left(\frac{\lambda}{N_A\, h\, c}\right) \tag{20}$$

such that $R_d = k_d[In]$, and the rate of initiation, $R_i = 2R_d$.

Here, $[In]$ is the concentration of the initiator, I_0 is the incident intensity of the light source, and I_{abs} is the absorbed intensity integrated up to z. In order to convert the intensity into moles of photons per unit volume, the wavelength of the light in nanometers, λ, Avagadro's number, N_A, Planck's constant, h, and speed of light c, were used. ϕ is the quantum yield of initiation, and it indicates the efficiency of a radical in initiating a polymerization event [25]. ϵ is the molar absorptivity of photons for a given initiator, it depends on the wavelength and temperature, and it can be determined experimentally by measuring the absorption for known quantities of initiator concentrations in a solvent of known absorption [25]. The combined term k_d can also be experimentally determined from the half life of the initiator and the rate of change of initiator concentration, as shown in Equations (21)–(23) [25]. Typically, values of k_d for photoinitiated radical polymerization are in the range of 10^{-3}–10^{-1} mol/m^3-s [25].

$$[In] = [In]_0 e^{-k_d t} \tag{21}$$

$$ln\left(\frac{[In]}{[In]_0}\right) = -k_d t \tag{22}$$

When half of the initiator concentration is consumed, the time is $t_{1/2}$. Using this information, k_d can be calculated as follows:

$$k_d = \frac{0.693}{t_{1/2}} \tag{23}$$

The rates of propagation and termination are affected by diffusion limitations and thus they may vary at different times during the reaction. In order to determine these variations in the reaction rate constants, a critical free volume parameter, f_{ct}, can be used. This dependence is used by Goodner *et al.* in describing the rate constants for propagation and termination, as shown in Equations (24)–(25) [9].

$$k_p = \frac{k_{p0}\, exp(-E_p/RT)}{1 + exp(A_p(\frac{1}{f} - \frac{1}{f_{cp}}))} \tag{24}$$

$$k_t = k_{t0} exp(-E_t/RT) \left(1 + \frac{1}{R_{rd}\, k_p[M]/k_{t0}\, exp(-E_t/RT) + exp((-A_t(1/f - 1/f_{ct})))}\right)^{-1} \tag{25}$$

In the above analysis, it is assumed that there is no oxygen in the system, so the rate constant for oxygen quenching is zero. The constants "k_{p0} and k_{t0} are the pre-exponential factors for the true kinetic constants" [9]. When the fractional free volume, f, of the system is greater than the critical free volume, f_{ct}, the polymerization is reaction limited, and when the fractional free volume is less than the critical free volume, the polymerization is diffusion controlled. The constants E_p, E_t, A_p, A_t and R_{rd} are parameters specific to the particular monomer.

Differential photocalorimetry (DPC) is a method used to measure the instantaneous heat generated during a reaction. By relating the heat generated to the propagation rate, rate constants, the rate constants k_p and k_t can be isolated. Continuous irradiation experiments are run to estimate the ratio of $k_p/\sqrt{k_t}$ and flash exposure experiments are run to estimate the ratio k_t/k_p from the dark reactions. By combining these measurements, k_p and k_t are determined independently at various conversion levels for a specific temperature [28]. This data can be used to estimate the constants

in Equations (24) and (25). By applying the simplifying assumptions that there is continuous irradiation with no oxygen, and the total live radical concentration is at steady state (when the rate of initiation equals the rate of termination) Equations (11)–(16) can be condensed. Using the simplified equations, the radical concentration and change in the monomer concentration with respect to time can be described as shown in Equations (26) and (27).

$$[R\bullet]_{ss} + [P\bullet]_{ss} = \sqrt{\frac{k_d[In]}{2k_t}} \tag{26}$$

$$\frac{d[M]}{dt} = k_p\sqrt{\frac{k_d[In]}{2k_t}}[M] \tag{27}$$

The double bond conversion, α, of multifunctional monomers, can be calculated with Equation (28). $[M]$ is usually the concentration of monomers in the in the system, but when finding double bond conversion, $[M]$ needs to be multiplied by the number of functional groups.

$$\alpha = \frac{[M]_0 - [M]}{[M]_0} \tag{28}$$

The rate of monomer disappearance, $R_p = \frac{-d[M]}{dt}$, is related to the exotherm of the reaction. The value of [M] at any point in the reaction can be determined from the heat removed, which is proportional to double bond conversion. The quantity $k_p/\sqrt{k_t}$ shown in Equation (29) is calculated, assuming the radical concentration is at steady state.

$$\frac{k_p}{\sqrt{k_t}} = \frac{-d[M]/dt}{\sqrt{k_d[In]}[M]} \tag{29}$$

By analyzing the reaction occurring in the DPC pan after the light has been turned off, (i.e. $k_d = 0$), the ratio k_t/k_p can also be defined using a combined variable for all live radicals in the system, $P^*\bullet$:

$$[P^*\bullet] = [P\bullet] + [R\bullet] \tag{30}$$

Using this combined variable $P^*\bullet$, Equations 12, 13 and 14 can be combined to get:

$$\frac{[dP^*\bullet]}{dt} = -2k_t[P^*\bullet]^2 \tag{31}$$

$$\frac{d[M]}{dt} = -k_p[M][R\bullet] - k_p[M][P\bullet] = -k_p[M][P^*\bullet] \tag{32}$$

Rearranging Equation (32) by using $[P^*\bullet]$ gives

$$[P^*\bullet] = \frac{-d[M]/dt}{k_p[M]} = \frac{R_p}{k_p[M]} \tag{33}$$

Integrating Equation (31) after plugging in Equation 33, one gets

$$\frac{[M]}{R_p} = -2\frac{k_t}{k_p}t + \frac{[M]_0}{R_{p0}} \tag{34}$$

Therefore, the slope of the plot of $[M]/R_p$ vs. time equals $-2k_t/k_p$. From these two ratios, namely $k_p/\sqrt{k_t}$ and k_t/k_p, the values of k_p and k_t can be independently determined. In one such experiment for a system of DMPA as the initiator, and the tetraacrylate monomer ethoxylated pentaerythritol tetraacrylate (E4PETeA), k_p values in the range of 0.04 to 15 $m^3/mol\text{-}s$ over various temperatures were reported [28]. Similarly, the values of k_t for the same system were between 0.3 to 3900 $m^3/mol\text{-}s$ [28]. In general, the values of k_p for free radical polymerizations are between 10^{-1} and 10 $m^3/mol\text{-}s$, and those for k_t are in the range of 10^3 to 10^5 $m^3/mol\text{-}s$ [25].

In a technique known as pulsed laser polymerization–size exclusion chromatography (PLP-SEC), k_p and k_t can be determined independently by exposing the sample to short pulses of light [25]. With each pulse of light, free radicals are generated, and when the light is turned off, propagation dominates due to the relatively large number of monomers in comparison to the radical concentration. Subsequent pulses of light on the same sample can be used to determine the degree of polymerization associated with each pulse of light, labeled L_i in Equation (35).

$$L_i = ik_p[M]t_p \tag{35}$$

Here, i refers to the cycle of the pulse, and t_p indicates the time of the pulse. The degree of polymerization for the chains that have propagated through i pulses, L_i, is determined from the SEC measurement of the polymer molecular weight distribution, through which the value of k_p can be determined [25].

Loss of radicals to oxygen, known as oxygen inhibition, is a problem that is pervasive in polymerization involving radicals [6, 19, 25, 11, 24]. Oxygen competes strongly for the radicals to form a stable peroxy radical as seen in Equations (9) and (10). Until most of the oxygen in the reaction volume has been used up, via reaction with radicals, there is very little consumption of the monomer [6]. It is possible to either exclude oxygen by performing the reaction in a nitrogen purged chamber, or to minimize the oxygen diffusion into the sample once the reaction starts. One such method of minimizing oxygen diffusion is described by Lovestead *et al.* [19, 25], where they suggest that using a light source with different wavelengths might allow for quicker oxygen elimination. The lower wavelength, which can only penetrate a few microns deep into the sample, cures the top layer and seals off any additional oxygen diffusion into the sample. The higher intensity wavelength can then be used to cure the rest of the sample, which can proceed once the pre-dissolved oxygen is consumed.

2.2 Stochastic models

Kinetic Monte Carlo simulations, which determine the reaction sequence based on the probability of each possible event, can be used to predict the double bond conversion and also the molecular weight distribution and network connectivity. Since polymerization reactions can be considered as random events, using simulations in a large enough reaction volume should accurately reproduce the reactions in a bulk system [8]. Monte Carlo simulations are based on the Gillespie algorithm, which computes the probability for all possible reactions. The next reaction that will occur out of n possibilities in the reaction volume is selected from this probability distribution [8]. Random numbers ξ_1 and ξ_2 are used in this selection, as shown in Equation (37):

$$R_{tot} = \sum_{\nu=1}^{n} R_\nu \tag{36}$$

$$\sum_{\nu=1}^{\mu-1} R_\nu < \xi_1 R_{tot} \leq \sum_{\nu=1}^{\mu} R_\nu \tag{37}$$

The associated time τ required for this reaction to take place is given by Equation (38); thus both the reactions and a physical time can be predicted.

$$\tau = -\frac{ln(\xi_2)}{R_{tot}} \tag{38}$$

2.2.1 Stochastic spatial models

Lattice based models are often used along with random numbers to simulate a reaction volume when the spatial location of each reactant molecule is part of the desired output information, or necessary to model the reactions. The probability of reaction selection can be based on the free volume of the reactants, diffusion limitations present in the distance between reactants, or reaction rates of all the possible pairs, to name just a few possibilities. For instance, a sufficiently large lattice (determined via comparison of simulation results with the experimental data) with randomly positioned reactants is one example of the simulated reaction volume. Not all spatial models of photopolymerization calculate the physical time, and this is especially true of lattice based models which focus on the spatial position of all species rather than the physical time required for these molecules to move [1, 3, 13, 20, 30]. Early spatial stochastic models contained reactants at fixed positions on the lattice, and thus lacked mobility [20], but newer models have been developed to give the molecules more mobility, allowing both initiators and polymers to move between lattice points [30]. In some cases, the reactants are allowed to move away from the lattice sites, and assume intermediate distances determined through Lennard-Jones rules of attraction [13].

The first kinetic gelation model by Manneville *et al.* [20] was for co-polymerization with immobile species. The monoacrylate and diacrylate molecules each occupied a single lattice site. Instead of using a reaction rate to determine the number of initiators that should decompose, an active radical was selected at random and allowed

to move to an adjacent monomer site, which indicated a reaction. In this manner, molecules reacted and changed their status, although they never moved from their original positions.

In the lattice model described by Bowman *et al.* [3], the homopolymerization of diacrylates is simulated using a face centered cubic lattice to represent the reaction volume [3]. They incorporate some void sites, and in a break from the usual assignments, each monomer occupies three adjacent sites, and the initiator occupies two adjacent sites. All the species involved, namely the polymer, monomer, solvent and initiator, can move as long as there is an adjacent unoccupied site, and all bonds are preserved. Assigning each diacrylate to multiple lattice sites assures that each functional group gets the opportunity to react with a reactive center. The rules of reaction incorporated in this simulation state that a given reactive center can propagate with any one of the nearest functional groups, which includes double bonds on polymer chains propagating with other double bonds on chains. Although this model provides connectivity information, the spatial proximity is not realistic due to the constant distance between each site. This was not a particularly important aspect in this paper because it did not impact the predicted double bond conversion trend at various initiator decomposition rates.

Based on polymerization snapshots, Bowman *et al.* were able to arrive at the same value as the experimentally determined maximum conversion. They were also able to confirm the logic that in the earlier stages of reaction, the pendant double bonds (double bonds on diacrylates, with one double bond on that monomer already reacted) react more readily than the monomeric double bonds, but as the conversion increases, it is harder for the pendant double bonds to react due to effects such as shielding and trapping. Since the rate constants used in this model were proportional to each other, and not representative of a true time scale, a physically meaningful time was not calculated.

Wen *et al.* [30] describe a lattice based simulation which incorporates the calculation of a physical reaction time. The heterogeneous network formation which occurs during the polymerization of multifunctional monomers is simulated on a 40 x 40 x 40 simple cubic lattice, and they use simple rules of motion for the reacted molecules. Each one of the lattice corners represents a monomer or an initiator. At the start of the simulations, the user inputs the lattice size, initiator concentration, rate constants and the primary cyclization enhancement factor. The propagation rate constant in the simulations is related to the experimentally observed value, and once the initiators and monomers are randomly distributed on the lattice, the next active radical that will react is randomly selected, based on the sum of all the reactions it can have with its neighbors. These surrounding molecules can be functional groups, active radicals or non-reactive sites. Once the next active site is selected for reaction, the local reaction probabilities are used to determine which neighbor it will react with and the time step equation described earlier in the Gillespie algorithm is used to calculate the time required for that reaction. After the status of all the reacted molecules is changed, the time step is checked to see if decomposition of any initiators could have taken place simultaneously during the reaction, and the initiator decomposition is also updated.

Unlike the lattice model by Bowman *et al.* [3] described above, the difunctional monomers simulated in this model only occupy one lattice site and none of the molecules can move. By trying different values of initiation and cyclization enhancement, they arrive at the trends that lead to a heterogeneous network. They conclude that using a higher initiation rate will lead to a more uniform network due to the higher availability of active radicals. On the other hand, increasing cyclization which depends on factors such as the monomer length and flexibility of the chain increases the heterogeneity due to the formation of highly cyclized regions [30]. Both of these trends, however, lack comparison to experimental data and the location of

monomers on the lattice sites at equal spaces is not representative of the true reaction volume.

Hutchison *et al.* [14] present a model that utilizes the attraction between the molecules in a given reaction volume. The kinetic gelation model is applied to an off-lattice simulation, where a simple cubic array of spheres is simulated within a cubic volume with periodic boundary conditions. At the start of the simulation, the location of all the monomers is randomized based on minimizing the total energy of the system and this scheme is continued even after the reaction sequence is started. The distance between the reactive ends of each diacrylate monomer is specified using the Lennard-Jones potential energy function and the orientation of the spheres is random. Thus, the potential energy of a new position is compared with all the other possible events of that type, and the most probable event is selected with the aid of random numbers weighted by these potential energies. As the reaction progresses, the reaction volume contains several separate microgels, which are caused by a single active site reacting with a cluster of monomers. These clusters were observed in the previously described models as well, but due to the movement of the particles off the lattice, the microgels are more prominently visible. Here again, although the selection of events and movement of molecules, is based on a Monte Carlo method, the physical time outlined in the Gillespie algorithm is not calculated.

2.2.2 Non-spatial stochastic models

One of the first models to use the Gillespie algorithm for a polymer system without a lattice was described by Kurdikar *et al.* [16]. This system also involved multi-functional monomers, and thus diffusion limitations caused by crosslinking were an important factor. This effect was acknowledged by relating the initiator efficiency to the diffusion coefficients of the radicals. The diffusion parameters for the propagating monomers and polymers were related to conversion with a simple relation dividing

the diffusion of the monomer in polymer by the degree of polymerization of the polymer. In order to take into account the reactivity of all the functional groups of the diacrylate, they devised a series of 28 possible reactions that involved differently sized molecules.

The number of possible reactions would increase as the functionality of the monomer increased. To account for different diffusion effects encountered by the monomers based on their chain length, the diffusivity of each monomer was normalized with its chain length. Although this model does not account for the distances between the reactants, it keeps track of which chain contains each monomer, as well as the status of each monomer. The extensive reaction event list enumerates all possible reactant pairs. This could be a lengthy list depending on the functionality of the monomer. One of the assumptions made in this model is that there are no primary radicals in the reaction volume. The instantaneous decomposition of an initiator molecule is recorded by the change of two monomers into two activated monomers. This chemistry is not necessarily true as it ignores the termination of primary radicals which can occur when propagation reactions are not favorable. The system sizes used in this model are significantly higher than those in the lattice based models. This model had ten million monomer molecules, and an additional 100,000 initiator molecules which equaled 1% initiator. Using the simulation results they were able to demonstrate that as the intensity of the light source increases, the rate of conversion increases. They were also able to show theoretically the number of radicals present in the simulation volume throughout the entire reaction time. Since they did not aim to compare their results to experimental data, the model is simply presented as a tool which can be used to generate multiple realizations to obtain quantitative predictions.

Models that use population balance equations are another example of stochastic connectivity models that do not track spatial information. Population balance equations (PBE) are a series of dynamic differential equations that track the different

properties of each species such as chain length (molecular weight), number of branch points, and number of radicals on each chain. The complexity of the PBE increases as the number of identifying characteristics for each species increases. Several different numerical methods are used to manage the large number of differential equations in such cases.

2.3 Models used in this thesis

The kinetics of the polymerization reactions can be determined from ODE rate equation models, such as the ones described in Equations (11)–(16), by fitting them to experimental conversion data. However, the use of these kinetics to predict part height may depend on more than the double bond conversion, when the intensity of light, or the initiator concentration is varied. Although the double bond conversion predicted by the ODE model and the KMC model are identical, the ODE model lacks connectivity information and it cannot be used to compute the molecular weight for multifunctional monomers. Results from a stochastic KMC model, which is capable of predicting network connectivity information of the resulting polymer, are shown in Chapter 3.

The ODE model presented here includes the initiation, propagation, termination and inhibition mechanisms shown in Equations (1)–(10). One-dimensional oxygen diffusion in the vertical direction is also included to simulate the mobility of oxygen toward areas that are depleted of oxygen as the reaction progresses. In addition to the ODEs presented in Equations (11)–(16), a modification to Equation (16), using the diffusion coefficient D_{oxy} of the oxygen in monomer, accounts for the oxygen diffusion, as shown in Equation (39).

$$\frac{d[O_2]}{dt} = -k_{toxy}[O_2][R\bullet] - k_{toxy}[O_2][P\bullet] - D_{oxy}\frac{\partial^2[O_2]}{\partial z^2} \tag{39}$$

The rate constants used in subsequent part height predictions, were determined by fitting conversion from the ODE solutions to available deoxygenated, and oxygenated,

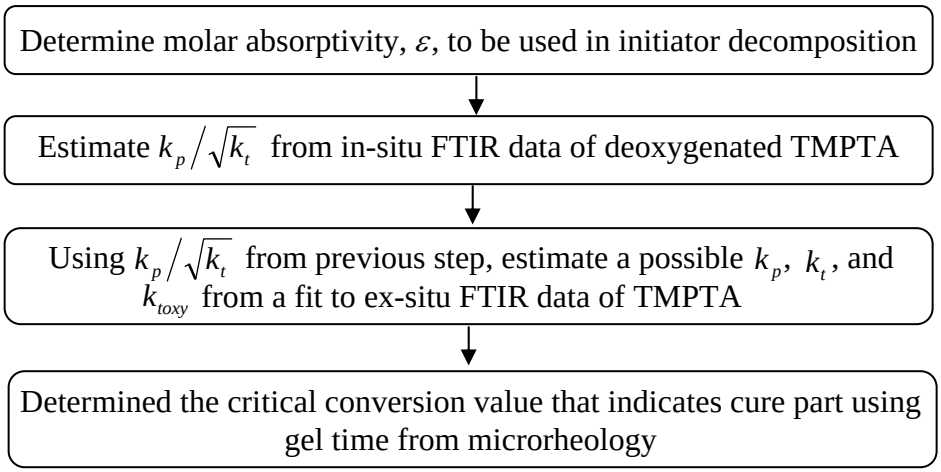

Figure 4: Flow chart of ODE model development

FTIR experimental data as described in Chapter 3. This process is outlined in Figure 4.

These rate constants were also used in the KMC model to predict more information about the system such as molecular weight evolution with time. Earlier stochastic models have described conversion and/or molecular weight, but not always with a physical time, as discussed in Chapter 1 [1, 3, 13, 20, 30, 16]. Population balance equations can be combined with KMC principles to predict molecular weight, but the complexity increases with each added index (molecular weight, conversion, number of radicals on each chain, etc.) [12, 21]. The KMC model used here is capable of handling both homo- and hetero-polymerization. Although the scope of this project is based on photo-polymerization, both the KMC model and ODE based model can be adapted to other polymerization processes by changing the rate mechanisms and rate constants. At the beginning of the simulation, the reaction volume was determined based on the desired number of monomers (system size), and the quantities of all other species were determined. The reaction rates of all the events in this discretized system were computed using the rate constants and the number of reactants. Using Equations (37) and (38) the next reaction event and the next set of reactants were selected, and the time required for this reaction was computed. The species tracked in the model

included the number of monomers, polymer chains, free double bonds, free radicals, initiators and oxygen molecules. Using the number of polymer chains, the number average molecular weight, weight average molecular weight, and molecular weights excluding the largest chain in the reaction volume were computed. The connectivity information stored included the number of radicals on each chain, and also which chain contained each monomer. Since the model is non-spatial, the assumption of a well-mixed reaction volume is required and this limits predictions to the early conversion regime. In the scope of this project, the desired information is until the onset of cure, and therefore the well mixed assumption does not hinder the part height prediction.

CHAPTER III

ESTIMATION OF KINETIC PARAMETERS

There are four unique rate constants in the ten mechanisms shown in Equations (1)–(10): rate of initiator decomposition, k_d, rate of propagation, k_p, rate of radical termination, k_t, and rate of radical termination via oxygen quenching, k_{toxy}. If it is assumed that the rate constants are unaffected by chain length at early conversion up to gelation, the rate constants for all the propagation, termination and inhibition reactions would be the same. In the case of termination, two possible mechanisms, termination via combination or termination via disproportionation are generally possible. However, in vinyl monomers, termination occurs mostly via combination, which is modeled here [22].

The rate of initiator decomposition, R_d, given in Equation 19, was determined from a combination of parameters that we measured and from parameters from literature references. This is detailed in Section 3.2. In Section 3.5 the coupled ODEs, described in Equations (11)–(15) and Equation (39), were used to estimate propagation, termination and inhibition rate constants from available FTIR experimental data.

3.1 Materials

2(2-ethoxyethoxy) ethyl acrylate (EEA, SR®256) and trimethylolpropane triacrylate (TMPTA, SR®351) were obtained from Sartomer®. The photoinitiator 2,2-dimethoxy-1,2-diphenylethan-1-one (DMPA, IRGACURE®651) was obtained from Ciba Specialty Chemicals®. It should be noted that 125 ppm of Hydroxy Quinone or 175 ppm of MEHQ are included in the formulation of EEA and TMPTA to inhibit polymerization from hydroxy radicals while in storage, and the inhibitor was

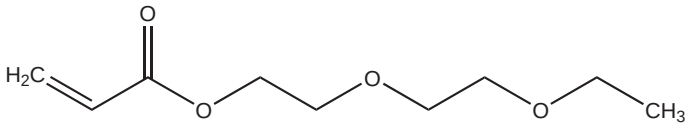

2(2-ETHOXYETHOXY) ETHYL ACRYLATE

Figure 5: The monofunctional acrylate used in this work is SR®256 (EEA)

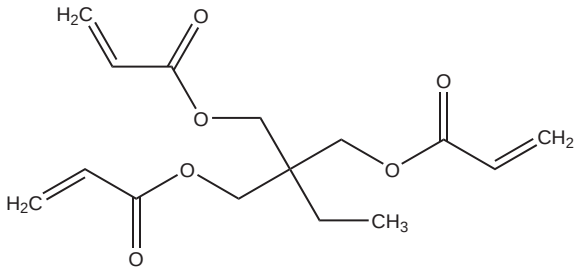

TRIMETHYLOLPROPANE TRIACRYLATE

Figure 6: The trifunctional acrylate used in this work is SR®351 (TMPTA)

not removed in the experiments, unless specifically noted. The above ppm concentrations are equivalent to the molar concentration of oxygen in the sample, but the exact amount of inhibitor in the monomer at the time of use can vary, and it has been shown that these inhibitors do not impede the photopolymerization as strongly as oxygen does [26]. All experiments were neat solutions (containing no additional solvent) of EEA and TMPTA prepared at varying initiator concentrations (1, 5 and 10 % w/w for EEA, and 0.5, 5 and 10 % w/w for TMPTA).

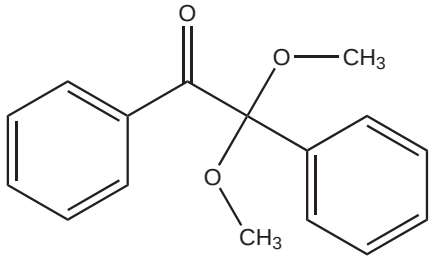

2,2-Dimethoxy-1,2-diphenylethan-1-one

Figure 7: The photoinitiator used in this work is IrgaCure®651 (DMPA)

3.2 Decomposition kinetics of DMPA

The rate of initiator decomposition for photopolymerization, R_d, from Equation 19, depends on the concentration of initiator, the intensity of the light source, and the depth into the absorbing medium [25]. The relationship between the rate constant k_d and all these variables was described in Section 2.1 using Equation (20), which is shown here again as Equation (40). The quantum efficiency, ϕ, is a value between 0 and 1 that describes the efficiency of radicals in initiating polymerization events. In the present case, ϕ was assumed to be 0.6 since that is a typical value for photoinitiators [10]. The molar absorptivity of the initiator, ϵ, is a parameter that can be determined experimentally by measuring the absorptivity of TMPTA solutions with various DMPA concentrations.

$$k_d = 2.3\phi\epsilon I_0 e^{(-2.3\epsilon[In]z)} \left(\frac{\lambda}{N_A\, h\, c}\right) \tag{40}$$

The absorbance was measured using a Cary spectrophotometer at 365 nm in disposable cuvettes. First, a cuvette filled with pure monomer was used to determine the baseline absorbance. Then, three different solutions of DMPA in TMPTA were prepared at the low concentrations of 0.067, 0.10 and 0.13 wt% , and the absorbance of each one of these solutions was measured separately. Absorptivity, A, equals $-log_{10}(I/I_0)$ and Equation (41) shows the relationship between absorbance and initiator concentration. Based on Equation (41), the data from the spectrophotometer is plotted in Figure 8, as absorbance versus initiator concentration. The absorptivity can be derived from the slope using Equation (41), and the path length through the sample, z, which is 1 cm for the cuvette. The final value for the molar absorptivity of DMPA obtained from these experiments was 15 m^2/mol, which was consistent with reports of 15 m^2/mol by other sources [2, 10, 28].

$$A = -log_{10}(I/I_0) = \epsilon[In]z \Rightarrow \epsilon = \frac{A}{z[In]} = \frac{slope}{z} \tag{41}$$

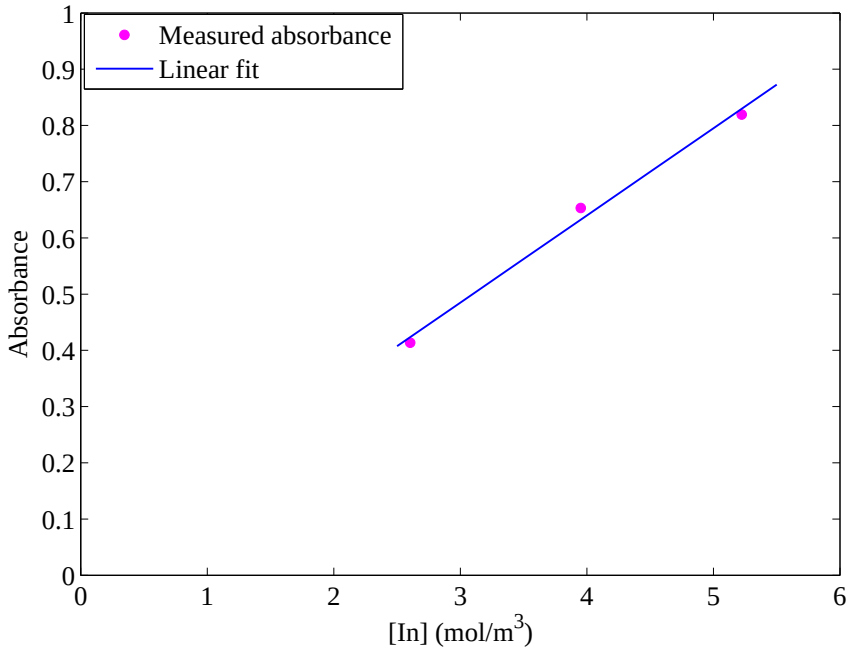

Figure 8: Molar absorptivity of DMPA at 365 nm

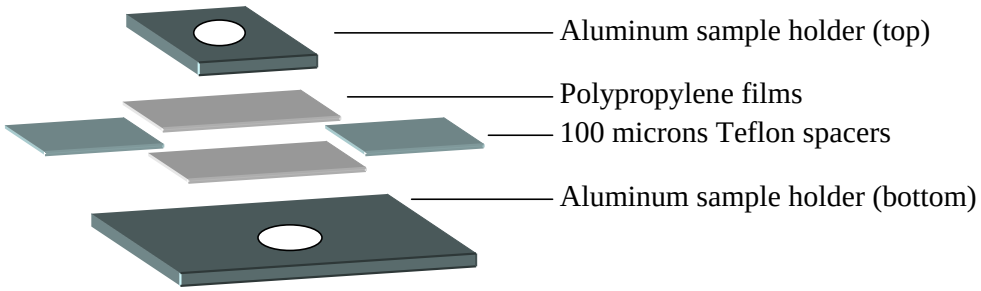

Figure 9: Schematic of the sample holder used in the FTIR experiments.

3.3 Measurement of double bond conversion with FTIR

3.3.1 In-situ FTIR data with deoxygenated TMPTA

Real time FTIR data from Lee *et al.* [18] for deoxygenated TMPTA with 1 wt%, DMPA was used to estimate $k_p/\sqrt{k_t}$ for TMPTA. The experimental methods are described elsewhere [18]. The data is shown in Figure 14, along with a comparison to the model.

3.3.2 Ex-situ FTIR of EEA and TMPTA

The ex-situ transmission-FTIR experiments to obtain double bond conversion α were performed by Dr. Santosh Rahane at Georgia Institute of Technology. A sample holder, such as the one shown in Figure 9, was made of two aluminum slabs with concentric holes, and it was used to expose the monomer solutions to UV-light and to perform FTIR characterization. First, two polypropylene films with a thickness of about 65 μm each, separated by a 100 μm thick Teflon® spacer, were clamped between the two aluminum slabs. Second, uncured monomer solutions with different initiator concentrations were transferred to the space between the polypropylene films using a pipette. Third, the samples were exposed to UV-light at 365 nm, at the light intensity of 140 W/m^2 on a Spectra-Physics 1000 W Hg lamp, for a desired exposure time. After exposure, the photopolymerized samples were analyzed using a Brucker FTIR instrument operated in transmission mode. The design of the sample holder allowed both photopolymerization, and FTIR characterization in the same setup without removing the polypropylene films from the aluminum slabs. A total of 100 scans were collected at a resolution of 4 cm^{-1} to compile the absorbance spectrum. The double bond conversion was measured using the ratio of areas under the C=C peaks (PAR) at 1625 cm^{-1}, to the C=O peak at 1720 cm^{-1}. Since the peak corresponding to asymmetric carbonyl stretching does not change during photopolymerization, it acts as an internal standard in the FTIR analysis. The equation used to compute the double bond conversion is given in Equation (42):

$$\alpha = 1 - \frac{PAR_t}{PAR_{t=0}} \tag{42}$$

where PAR_t is the peak area ratio at exposure time t, and $PAR_{t=0}$ is the peak area ratio for the uncured resin. Figures 10 and 11 show the data obtained from these experiments.

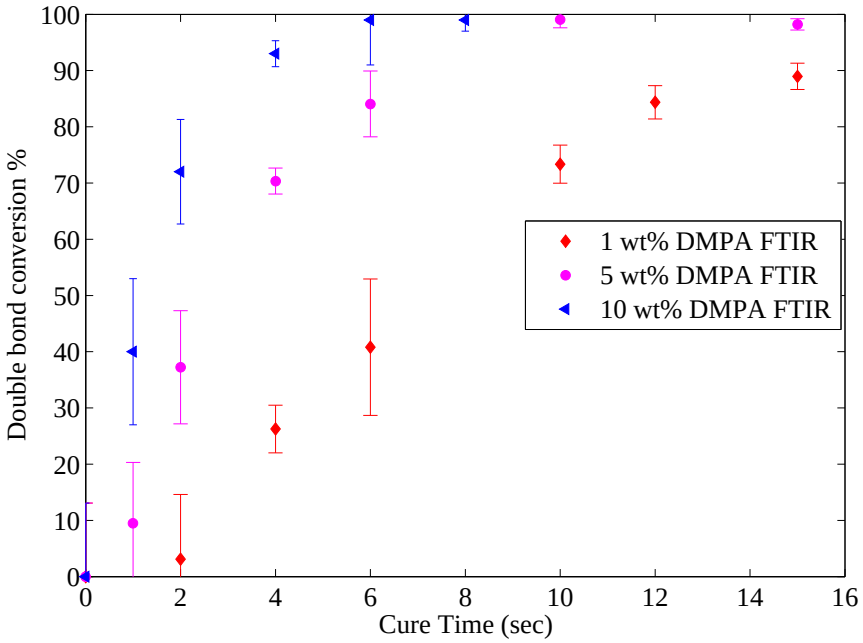

Figure 10: Ex-situ FTIR data for EEA

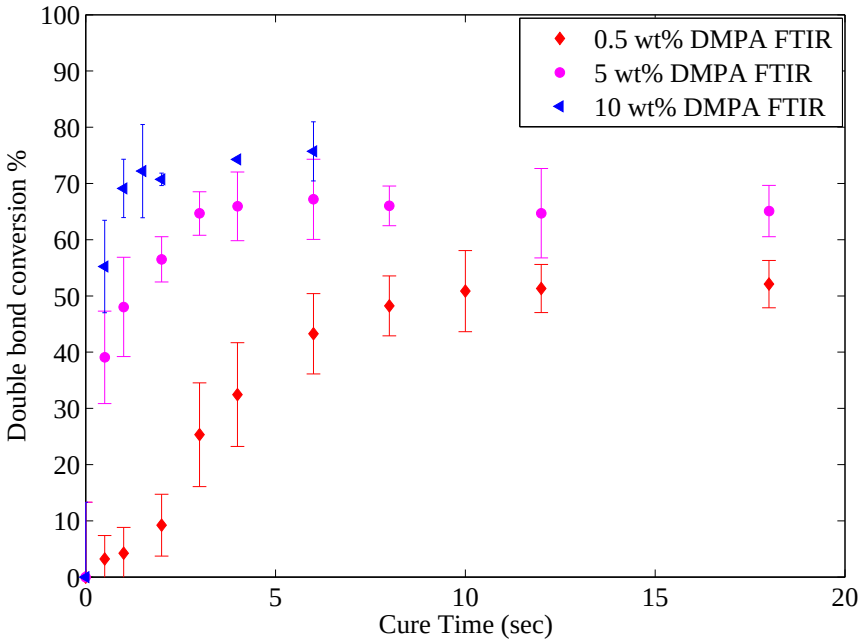

Figure 11: Ex-situ FTIR data for TMPTA

3.4 Simulating polymerization and oxygen diffusion

The double bond conversion data from FTIR shown in Section 3.3 is the average double bond value through the entire thickness of the sample. In order to simulate this polymerization using the ODE model, the simulated reaction volume was divided into thin layers as shown in Figure 23. The reaction volume in each one of these layers was assumed to be well-mixed, and the polymerization in each one of the layers was calculated. Oxygen was allowed to diffuse between the layers, and it was ensured that the diffusion length of oxygen in TMPTA was greater than the slice thickness used in the simulations. The resulting double bond conversion value in each one of these slices was averaged, to obtain an average double bond conversion for the entire sample volume comparable to the experimental data. When dealing with ex-situ experimental data, the simulation was allowed to run for a minute after the time of exposure, while the rate of initiator decomposition was set to zero, to simulate "dark reactions" where any remaining live radicals could propagate or terminate with surrounding double bonds. The following sections contain a detailed description of the rate constants obtained by fitting the simulated double bond conversion to experimental double bond conversion data from FTIR.

3.5 Estimating rate constants from fit to experimental data

3.5.1 Fit to monoacrylate data

Rate constants were fit to the FTIR conversion data, shown in Figure 10, for monoacrylates, using the double bond conversion values obtained from a model based on Equations (11)–(15) and Equation (39). To simulate the reaction volume, the 100 μm simulated vat was divided into ten layers, each with a thickness of 10 μm. The simulated vat was 100 μm deep because of the 100 μm spacer used in the ex-situ FTIR experiments. Oxygen diffusion in one dimension between these slices was also included. As a result of this discretization, each slice had a different conversion, and

oxygen concentration value. The average double bond conversion was obtained by averaging over all the slices. In addition to the oxygen effect and discretization of the reaction volume, dark reactions were included when simulating data to match ex-situ experimental data. Dark reactions are propagation and termination reactions that occur between any remaining active radicals when the light is turned off, which means k_d=0. To estimate rate constants, k_p, k_t, and k_{toxy}, by fitting to the experimental data, an optimization algorithm in MATLAB® called pattern search was used along with the above model. The optimization routine minimized the root mean square error (RMSE), which was computed using the experimental data y, and the predicted data $\hat{y}$ in Equation (43). During this analysis, several different combinations of k_p and k_t were found to provide an equally good fit to the data, as shown in Figure 13, and all these combinations had the identical $k_p/\sqrt{k_t}$ value of 0.3135 $(m^3/mol\text{-}s)^{0.5}$. This is consistent with the analysis of continuous reactions in Section 2.1 where the importance of $k_p/\sqrt{k_t}$ was highlighted. As it was shown there in Equation 29, only $k_p/\sqrt{k_t}$ can be isolated from an analysis of continuous reactions, but another data set, such as one measuring dark reactions, is necessary to separately identify k_p and k_t.

$$RMSE = \sqrt{\frac{\sum_{i=1}^{n}(y_i - \widehat{y}_i)}{n}} \tag{43}$$

Table 1: Parameters used in estimating rate constants for EEA and TMPTA

Parameter	Value	Units	Source
ϕ	0.6	–	[10]
ϵ	15	m^2/mol	Figure 8
Intensity, I_0	140	W/m^2	Measured
$[O_2]_0$	1.05	mol/m^3	[11, 24]
Diffusion coefficient for O_2	1e-10	m^2/s	[24]
Molecular weight EEA	188	g/mol	Sartomer
Molecular weight TMPTA	296	g/mol	Sartomer
Molecular weight DMPA	256	g/mol	Ciba

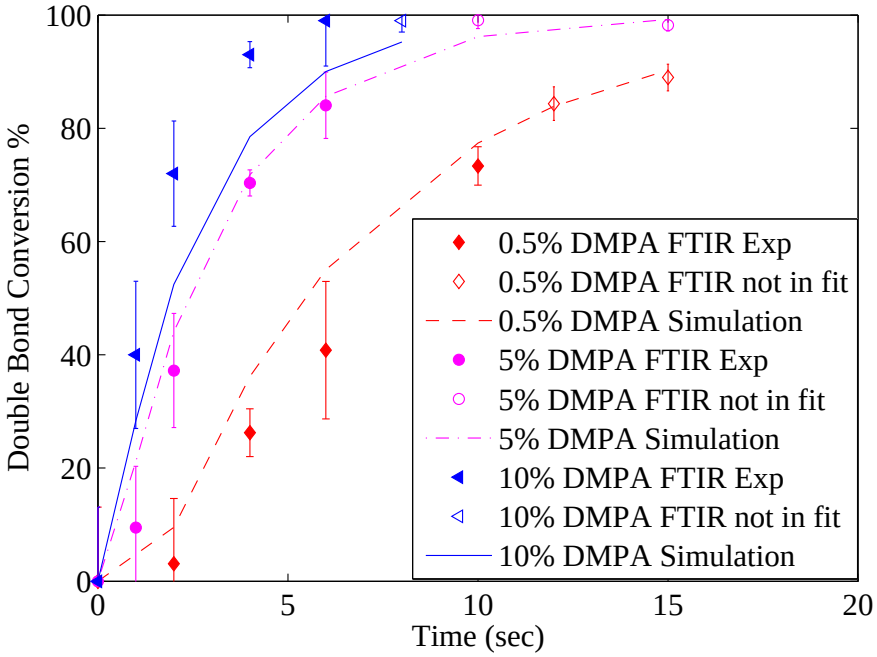

Figure 12: Fit to monoacrylate IR data shows that the best fit $k_p/\sqrt{k_t}$ is 0.3135 $(m^3/mol\text{-}s)^{0.5}$. Here, $k_p = 9.6$, $k_t = 937.9$, and $k_{toxy} = 285500$. All the rate constants have units of $m^3/mol\text{-}s$.

3.5.2 Fit to in-situ FTIR data of deoxygenated TMPTA

Monoacrylate conversion data reaches high conversions, close to 100%, unlike the TMPTA data shown in Figures 11 and 14. Cross-linking in multifunctional acrylates causes the onset of gelation at early conversion, which leads to mobility issues, thus preventing full double bond conversion. Therefore, the rate constants are only fit to the early conversion data, which will in turn only describe the cure kinetics until the start of gelation.

The in-situ FTIR early conversion data for deoxygenated TMPTA, at 1 wt% DMPA and 365 nm light with an intensity of 140 W/m^2, obtained from Lee *et al.* [18], was used to estimate the ratio of $k_p/\sqrt{k_t}$ to be 0.4146 $(m^3/mol\text{-}s)^{0.5}$. The experimental data points selected to be used in the fit were double bond conversion values, less than 15 %, measured before the effects of gelation impacted the rate of conversion. As it can be seen from Figure 14, the double bond conversion curve

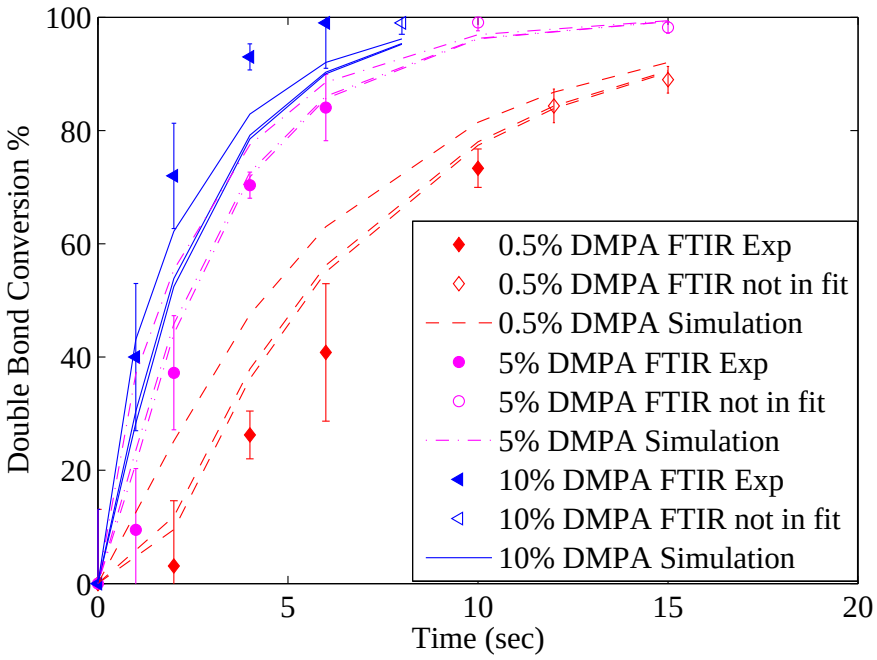

Figure 13: Changing k_p while holding $k_p/\sqrt{k_t}$ constant at 0.3135 gives equally good fit to the monoacrylate conversion data as long as $k_p > 5 m^3/mol\text{-}s$. The k_p values tested here are 1, 5 and 10, with 1 being the curve that is steepest. Once $k_p > 5\, m^3/mol\text{-}s$, the curves are nearly identical.

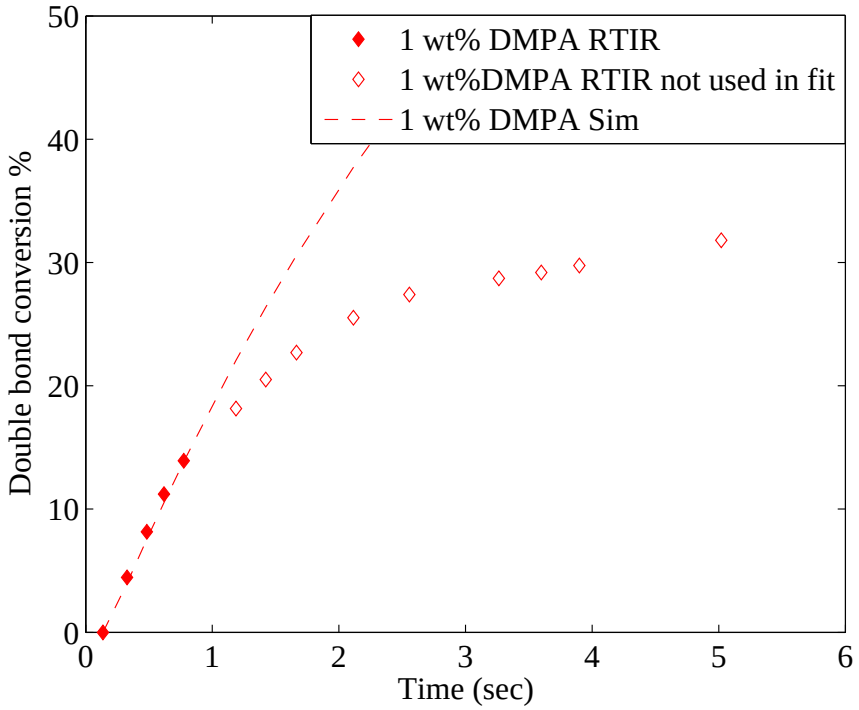

Figure 14: Rate constants fit to in-situ FTIR data of 1 wt% DMPA in deoxygenated TMPTA give $k_p/\sqrt{k_t} = 0.4146$. Experimental data from Lee *et al.* [18].

starts rising slower after reaching 15%. Another detail to mention is the fact that the original data set, from Lee *et al.* [18], contained some lag, and it did not contain a clear indication of when the reaction started. Thus, the data shown here has an estimated lag, which impacts the resulting k_p from this fit. Due to this, only the value for $k_p/\sqrt{k_t}$ was obtained from this data set. The sample depth in the experiments was only 15 μm, so the simulated vat was also 15 μm, and it was divided into 3 slices of 5 μm each. Dark reaction effects, and oxygen diffusion effects, were not included in the simulations because the experimental data was in-situ and the system was monomer was deoxygenated. Once again, the pattern search algorithm and Equation (43) were both used to obtain the best fit between the double bond conversion predicted by the ODEs and the selected experimental conversion data in Figure 14. As in the case of the monoacrylates, several suitable values of k_p could be used with the same $k_p/\sqrt{k_t}$, as shown in Figure 15.

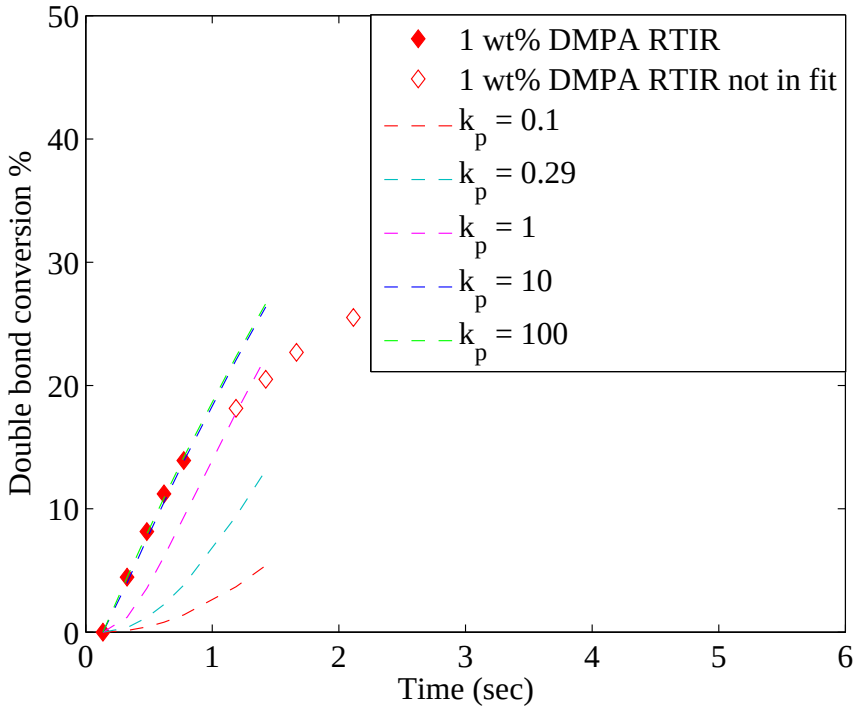

Figure 15: Changing k_p shows that for $k_p > 2$, the fit is equally good when $k_p/\sqrt{k_t}$ is held constant at 0.4146. All rate constants have units of $m^3/mol\text{-}s$. TMPTA experimental data from Lee *et al.* [18].

3.5.3 Fit to ex-situ FTIR data of TMPTA with oxygen

The ratio of $k_p/\sqrt{k_t}$, obtained for the triacrylate deoxygenated data, was used to fit to the ex-situ FTIR data and obtain a suitable set of k_p, k_t, and k_{toxy} values. To simulate the reaction volume, the 100 μm simulated vat was divided into ten layers, each with a thickness of 10 μm. The simulated vat was 100 μm deep because of the 100 μm spacer used in the ex-situ FTIR experiments. Oxygen diffusion in one dimension between these slices was included, and the diffusion length of oxygen over the time scale of the experiments was about 5E-5 m. Thus, the selected slice width of 1E-5 m was sufficient to prevent any addition of oxygen during reaction in each slice. As a result of this discretization, each slice had a different conversion, and oxygen concentration value. The optimization was constrained so that k_{toxy} should be greater than, or equal to, the rate constant for termination. The fit in Figure 16 is the best fit to all the experimental data sets for conversion values less than 60%. Again, the experimental data points selected to be used in the fit were points measured before gelation impacted the rate of conversion. This meant that for the lowest initiator concentration, the data points selected were all below 30% conversion, and the earliest data points for the higher initiator concentrations were already at, or above, 40% conversion.

Table 2: Estimated rate constants from all three data sets shown above.

Monomer	k_p $(m^3/mol\text{-}s)$	k_t $(m^3/mol\text{-}s)$	k_{toxy} $(m^3/mol\text{-}s)$	$k_p/\sqrt{k_t}$
EEA with O_2	9.6	937.9	285520	0.3135
TMPTA w/o O_2	1.61	14.34	–	0.4146
TMPTA with O_2	0.26	0.39	2	0.4146

All the rate constants estimated in Chapter 3 are summarized in Table 2. The difference in $k_p/\sqrt{k_t}$ between monoacrylates and triacrylates means that for the same k_p in both monomers, the monoacrylates will have higher rates of termination than the triacrylates. It is also important to note that although the $k_p/\sqrt{k_t}$ values are unique

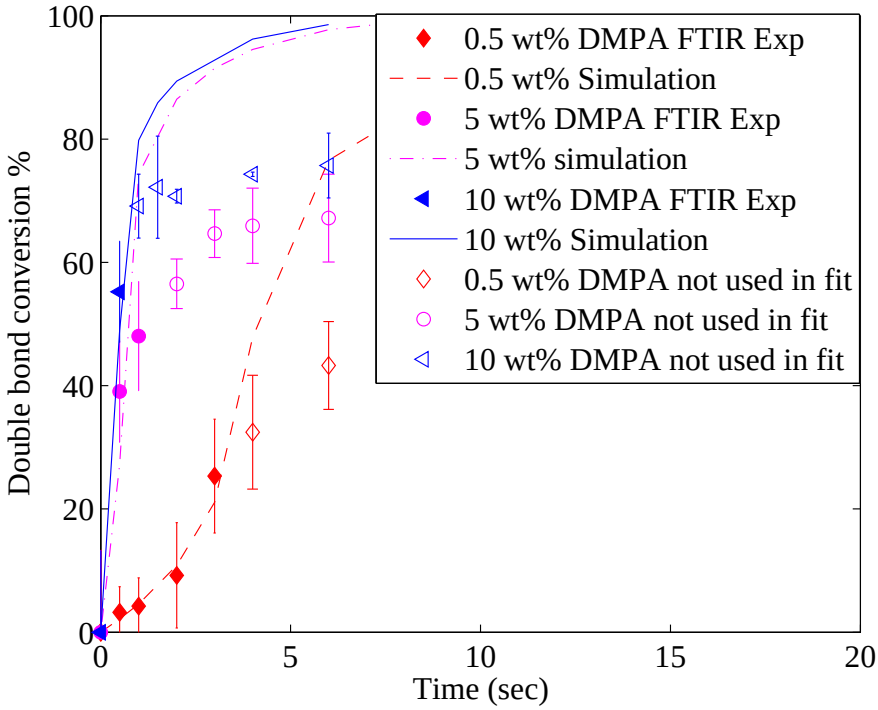

Figure 16: Best fit of rate constants to all three data sets of DMPA in TMPTA. The $k_p/\sqrt{k_t}$ used here is from the deoxygenated data set, and the optimization has been constrained so that the k_{toxy} is greater than or equal to k_t. Here, $k_p = 0.26\, m^3/mol\text{-}s$, $k_t = 0.39\, m^3/mol\text{-}s$, $k_{toxy} = 2\, m^3/mol\text{-}s$.

between the two triacrylate data sets, they don't have the same k_p and k_t values as the best fit. This is due to the fact that the deoxygenated data was extracted from a literature source and it is unclear how long the lag is in the deoxygenated data. Even if there is no lag due to inhibition, there might be some due to decomposition kinetics. By removing a portion of the lag, as has been done in the data shown in Figure 14, there is a need to use higher values of k_p to match the fast rise.

3.6 KMC simulations and comparison to GPC data

3.6.1 Molecular weight data from GPC

Gel Permeation Chromatography (GPC) is a method used to analyze a partially cured sample, and identify its average molecular weight. Solutions of 1, 5 and 10 wt% 2,2-Dimethoxy-1,2-diphenylethanone (DMPA) in EEA, and 0.5 wt% DMPA in TMPTA were pipetted into the space between two glass slides separated by a 100 μm Teflon® spacer. A schematic of the cure setup is shown in Figure 25. The solution was cured using a Spectra Physics Hg(Xe) lamp at an intensity of 140 W/m^2, with 365 nm UV light for varying exposure time periods. The cured samples were allowed to soak in tetrahydrofuran (THF) for 24 hours in order to extract all the monomer and low molecular weight oligomers that were not a part of the solid network. After soaking the sample for 24 hours, the THF was filtered to remove the solid particles, and the excess THF was evaporated using a rotating evaporator. This concentrated solution containing uncured monomers and lower molecular weight chains was injected into a Silicon based GPC column. In general, the time required for each chain to travel through the pores in the column depends on the size of the chain. The larger chains have more momentum and therefore come out fastest. The number average and weight average molecular weights of each sample are calculated in this manner.

Due to the loss of polymer which was of too high a molecular weight to be removed from the network, the accuracy of the molecular weight determined for TMPTA using

this method is questionable. The KMC simulation of TMPTA with oxygen in Figure 20, compares the molecular weight obtained from the GPC measurements of 0.5 wt% TMPTA to the simulated value.

3.6.2 KMC simulations for TMPTA

All the simulations in Section 3.5, use the model based on ODEs in Equations (11)–(15) and Equation (39). The estimated rate constants obtained in Section 3.5 were fit to available double bond conversion data, since the ODE based model can only predict conversion for multifunctional monomers such as TMPTA. In contrast, the KMC model described in Section 2.3 is capable of making molecular weight, and connectivity, predictions in addition to double bond conversion predictions. A comparison between the results from the ODE model and the results from the KMC model is shown in Figures 17–20. All of the KMC simulation results shown here are average values from three realizations, all with the same initial conditions except for the seeds that are used in the random number generator of each simulation. The mechanism of KMC simulations is outlined in Section 2. The use of random numbers in deciding the sequence of reaction events is shown in Equations (37)–(38). Figures 17 and 18 are for the deoxygenated TMPTA with the same system size (number of monomers in the reaction volume) but different k_p values. A comparison between the two shows that as k_p is increased, the effects of the system size become more apparent. Figure 19 serves as a complement to Figure 17, as they both have the same k_p but different system sizes. Once again, a comparison between the two shows that increasing the system size, while holding k_p the same, decreases the fluctuations between multiple realizations. Regardless of the system size, and the k_p value being used, the ability of the KMC to predict connectivity and molecular weight, unlike the ODE model, is apparent in all of the plots. Figure 20 shows the KMC simulation of TMPTA with oxygen, for 0.5 wt% DMPA.

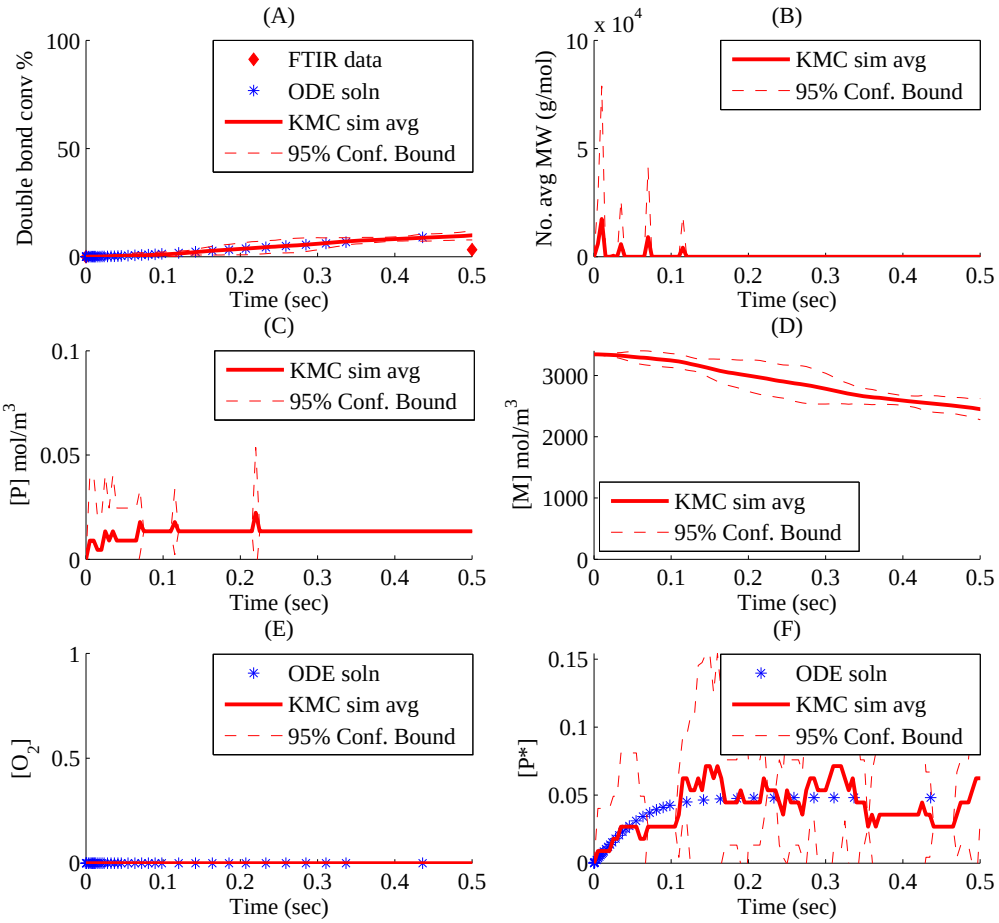

Figure 17: Results from a KMC simulation with a system size of 250,000 monomers of deoxygenated TMPTA compared to results from the ODE model and experimental data. $k_p = 5\ m^3/mol\text{-}s$ and $k_p/\sqrt{k_t} = 0.4146$; $I_0 = 140 W/m^2$, $\lambda = 365\ nm$, with 1 wt% DMPA. In-situ FTIR data is from Lee *et al.* [18] (A) The double bond conversion calculated from the KMC model matches the values from the ODE model in a multifunctional system. (B)&(C) Calculation of number average molecular weight requires knowledge of the total number of polymer chains. In a multifunctional monomer, only the KMC model can compute that information as seen in (C). In (B), the number average molecular weight excluding the largest molecule is shown here in order to replicate GPC data. Although $k_p/\sqrt{k_t}$ is sufficient to predict monomer conversion from KMC, molecular weight requires k_p and k_t separately. (D) The ODE model can only compute available free double bonds, not free monomer since it lacks connectivity information that KMC simulations provide. (E) $[O_2] = 0$ here but, the results from ODE and KMC simulations should match. (F) The average live radical concentration, $[P^*\bullet]$ from KMC and ODE simulations match. The fluctuations are due to system size effects which are exacerbated by higher values of k_p, which is 5 in this case. Here, the number of live radicals is about 4 at steady state.

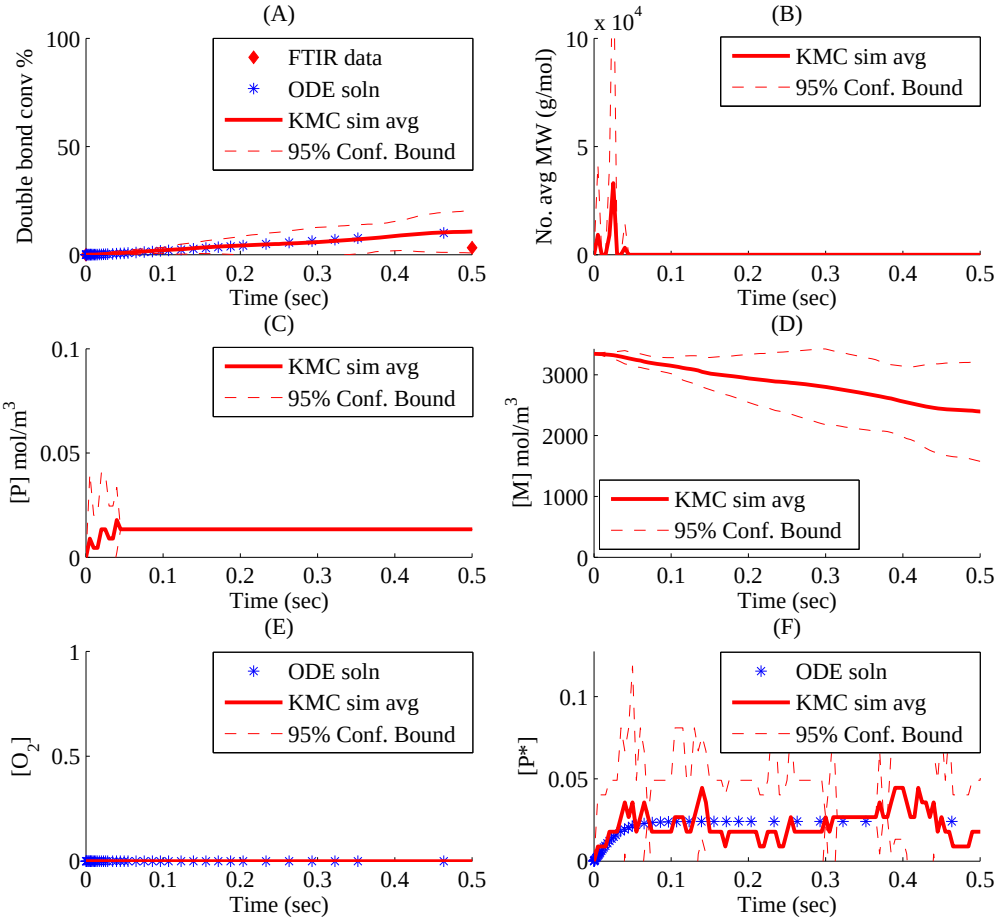

Figure 18: Results from 250,000 monomer system size KMC simulation of deoxygenated TMPTA compared to solution from ODE model. $k_p = 10\ m^3/mol\text{-}s$ and $k_p/\sqrt{k_t} = 0.4146$; $I_0 = 140 W/m^2$, $\lambda = 365\ nm$, with 1 wt% DMPA. In-situ FTIR data is from Lee *et al.* [18] (A) The double bond conversion calculated from the KMC model matches the values from the ODE model in a multifunctional system. (B)&(C) Calculation of number average molecular weight requires knowledge of the total number of polymer chains. In a multifunctional monomer, only the KMC model can compute that information as seen in (C). In (B), the number average molecular weight excluding the largest molecule is shown here in order to replicate GPC data. Although $k_p/\sqrt{k_t}$ is sufficient to predict monomer conversion from KMC, molecular weight requires k_p and k_t separately. (D) The ODE model can only compute available free double bonds, not free monomer since it lacks connectivity information that KMC simulations provide. (E) $[O_2] = 0$ here but, the results from the ODE and KMC models should match. (F) The average live radical concentration, $[P^*\bullet]$ from KMC and ODE simulations match. The fluctuations are due to system size effects which are exacerbated by higher values of k_p, which is 10 in this case. Here, the number of live radicals is about 1 at steady state.

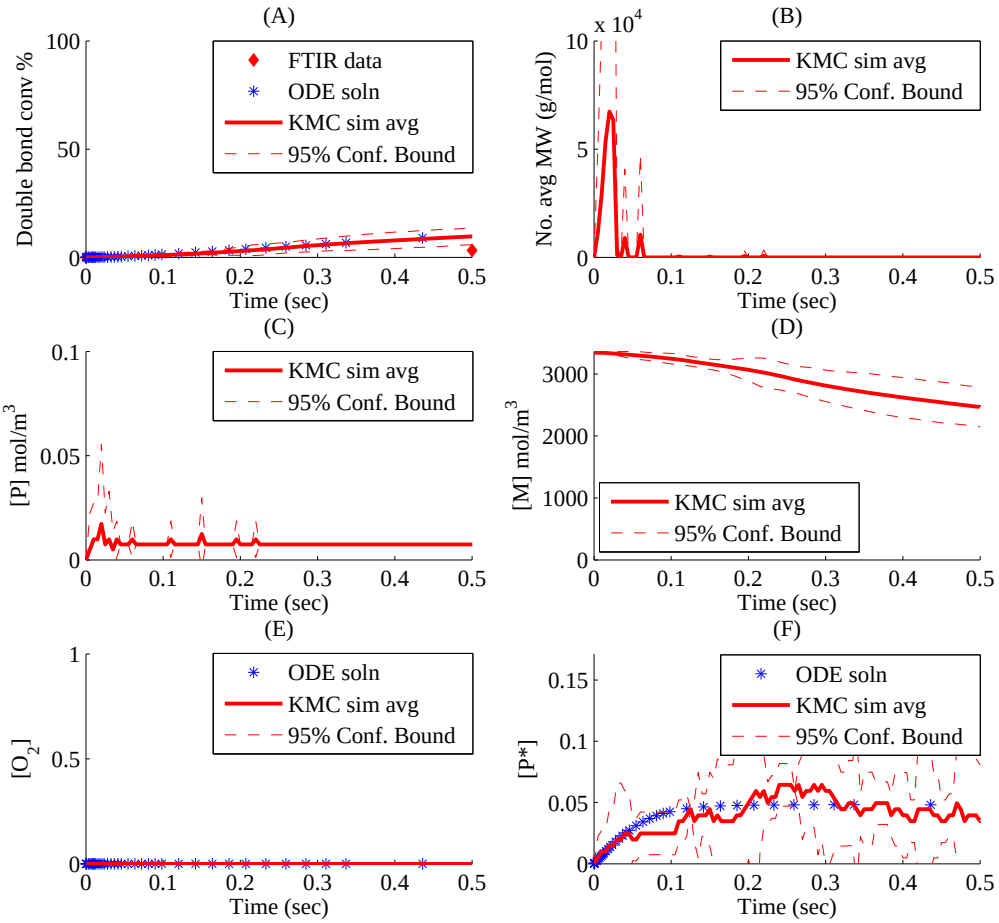

Figure 19: Results from 450,000 monomer system size KMC simulation KMC simulation of deoxygenated TMPTA compared to solution from ODE model. $k_p = 5m^3/mol\text{-}s$ and $k_p/\sqrt{k_t} = 0.4146$; $I_0 = 140W/m^2$, $\lambda = 365\,nm$, with 1 wt% DMPA. In-situ FTIR data is from Lee *et al.* [18]. The conclusions from plots (A)-(E) are still the same as from Figures 17 and 18, but the system size effects become apparent in comparing (F) in both cases. The average live radical concentration is higher, about 10 at steady state, and the fluctuations due to system size effects are visibly reduced.

Figure 20 highlights the necessity of having a unique k_p, in addition to the best fit $k_p/\sqrt{k_t}$ when matching molecular weight data. In the present work, KMC simulations are not utilized any further because a conversion cut-off value is adequate in process planning and determining cure height as seen in Chapters 4 and 5.

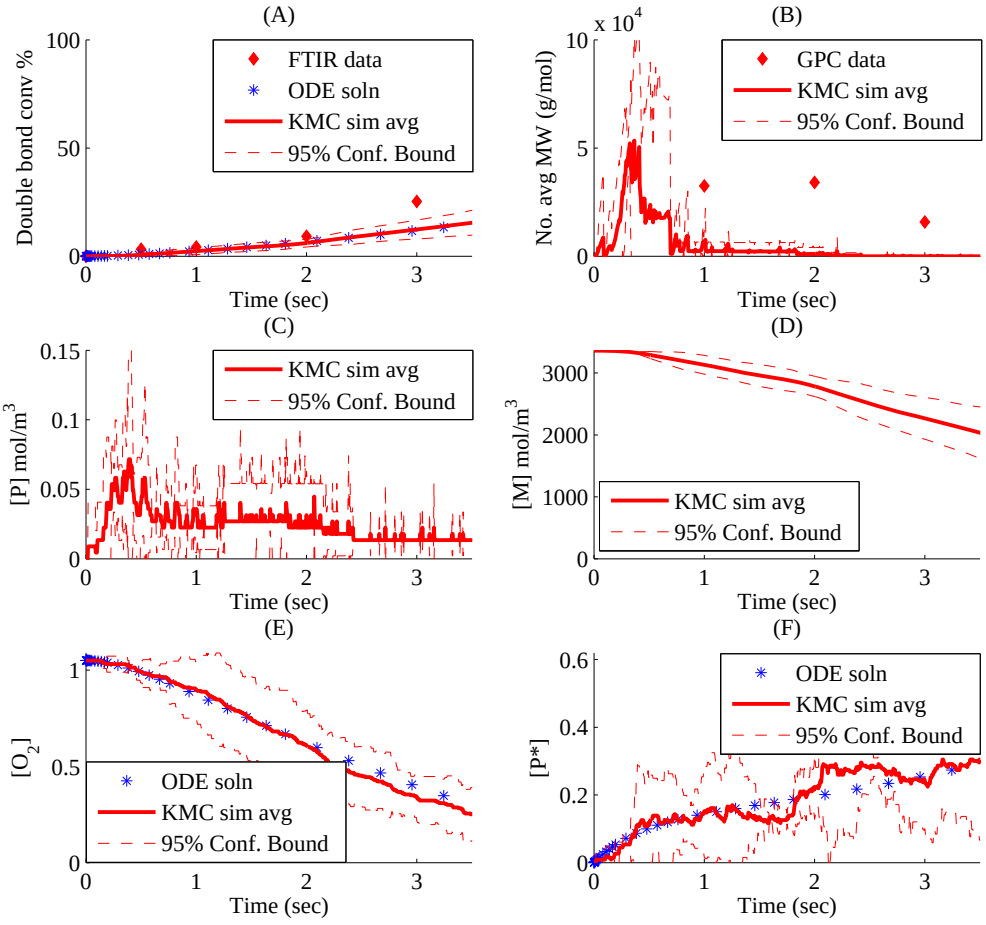

Figure 20: Results from 250,000 monomer system size KMC simulation KMC simulation of TMPTA with oxygen compared to solution from ODE model. $k_p = 0.26\ m^3/mol\text{-}s$, $k_t = 0.39\ m^3/mol\text{-}s$ and $k_{toxy} = 2\ m^3/mol\text{-}s$. $I_0 = 140 W/m^2$, $\lambda = 365\ nm$, with 1 wt% DMPA. The ex-situ FTIR data shown here is the same data shown in Figure 16. The conclusions from plots (A)-(E) are still the same as from Figures 17-19. The relatively small value of $k_p = 0.26\ m^3/mol\text{-}s$ means that there are more radicals generated and the number of live radicals, which is continuously rising reaches around 75 at the maximum time shown here. In comparison to the deoxygenated case, it is clear from this plot that having the oxygen inhibitor decreases the frequency of propagation reactions. The lower k_p used here, in comparison to the previous figures, reduces the fluctuations between different realizations.

CHAPTER IV

DETERMINING THE CONVERSION CUT-OFF USING GEL TIME DATA

Section 1.2 referred to the development of a versatile model that is capable of predicting cure height at various initial cure conditions. In Chapter 3, rate constants for the kinetic ODE model were estimated from available FTIR data for EEA and TMPTA. In this chapter, the kinetic ODE model with associated rate constants will be used along with experimental gel time data to determine a critical conversion value that can be used to predict part height.

Carothers and Flory described a gel as an infinitely large molecule that is insoluble [4, 5, 7]. Flory used this definition to estimate the degree of cure necessary for the onset of gelation, based on the functionality of the reacting monomers [7]. The estimated degree of cure differs in the cases with and without cyclization, and the equations for the two critical conversion values are shown in Equations (44)–(45). Once the resin starts to gel, the viscosity of the solution increases sharply, and the cure undergoes a rapid transition from a liquid state to a solid state [31]. Linear polymers, such as the ones formed by monoacrylates, usually undergo complete double bond conversion, and these polymers do not gel. In contrast, multifunctional monomers do not usually reach complete conversion of reactants due to the sharp increase in viscosity [26, 31]. The cross-linking described in earlier sections implies the dependence of onset of gel on the functionality of the monomer. In Equations (44)–(45) below, α_c and $\tilde{\alpha}_c$ are the critical conversion values, with and without cyclization, described by Flory as the conversion values that need to be reached before the resin can gel. α_c and $\tilde{\alpha}_c$ depend on the functionality of the monomer, f, which is

defined as the number of reactants each monomer can interact with. When a radical reacts with one end of a double bond, an active radical site is generated on the carbon at the other end. Therefore, in the case of the triacrylate, TMPTA, being using here, the functionality of each monomer is 6. Equation (44) is the critical conversion when there is no cyclization. In contrast, Equation (45) is the critical conversion predicted when there is cyclization. Since the focus in this project is on the early conversion regime, until the onset of gelation, Equation (44) is probably more relevant. Equation (44) is also more suitable in the scope of this project because all the samples are prepared without any solvent, and cyclization has been shown to be more significant in dilute systems [29].

$$\alpha_c = 1/(f-1) \tag{44}$$

$$\tilde{\alpha_c} = \sqrt{1/(f-1)} \tag{45}$$

Table 3: Theoretical critical conversion values for acrylates of various functionalities with and without cyclization.

	f	α_c	$\tilde{\alpha_c}$
Monoacrylate	2	∞	∞
Diacrylate	4	0.33	0.57
Triacrylate	6	0.20	0.44
Tetraacrylate	8	0.14	0.37

4.1 Gel time from microrheology experiments

Gel time experiments were performed by Dr. Ryan Slopek using microrheology, based on the premise of rapid change in the viscosity of a cross-linking polymer, and the procedure for these experiments is described elsewhere in more detail [26]. Briefly, particle tracking microrheology is a method used to determine the amount of time necessary to gel a monomer to a certain height. First, two glass slides separated by a 120 μm spacer were used to contain the sample solution, a pre-polymer with

nanoparticles. Subsequently, the sample solution was pipetted into the gap between the slides. The nanoparticles, which were well dispersed in the pre-polymer, moved due to particle vibrations, while their motion at a particular height was tracked using a high speed camera attached to a microscope. UV light at 365 nm, and various intensities, was used to cure the sample. The definition of "gel" used in the microrheology experiments was when the viscosity was sufficiently high to counteract the vibrations of the particles and they stopped moving. The time required for the onset of gel was recorded as the gel time. The experimental data for TMPTA is available at several initial conditions that are listed in Table 4. The conditions varied in these experiments include initiator concentration, $[In]$, intensity of the light source, I_0, and cure depth. All of these variables impact the initial rate of initiation, R_i, which is also shown in Table 4. R_i relates to the rate of decomposition, R_d, as $R_i = 2R_d$, because there are two radicals for each DMPA initiator molecule. Working curve plots used in traditional stereolithography models, such as the schematic shown in Figure 21, do not incorporate initiator concentration or intensity. In contrast, R_i can be used along with gel time to track the impact of initiation kinetics on gelation. Data from Table 4 is consolidated in this manner and is shown in Figures 22, 24, and 27 along with comparisons to the part height predictions from various models.

4.2 Estimating the critical conversion cut-off value by fitting to gel time data

If there is a fixed conversion value that defines the onset of gelation, the kinetics model can be used to compute the exposure time required to gel a part to desired height. This type of a degree of cure model is not usually used in stereolithography models, where the critical energy required to obtain the desired part height for a specific resin composition is determined through the E_c–D_p model:

$$C_d = D_p ln\left(\frac{E}{E_c}\right) \tag{46}$$

Table 4: Gel time data from microrheology experiments [26].

I_0 (W/m^2)	$[In]$ wt%	Depth of focus (μm)	$[O_2]$ (mol/m^3)	T_{gel} (s)	R_i (mol/m^3-s)
10	5	112	1.05	9	0.177
10	5	108	1.05	8.5	0.179
10	5	70	1.05	7	0.200
10	5	45	1.05	6	0.216
10	5	20	1.05	4	0.232
10	5	8	1.05	3	0.240
10	8	60	1.05	4	0.297
10	6.5	60	1.05	4.5	0.255
10	5	60	1.05	5.3	0.206
10	4	60	1.05	6.2	0.171
10	3	60	1.05	7.5	0.133
10	2	60	1.05	9.67	0.092
10	1	60	1.05	15.2	0.047
10	0.5	60	1.05	23.3	0.024
10	0.25	60	1.05	38.5	0.012
4	2	60	1.05	22	0.036
8	2	60	1.05	12.43	0.073
8	1	60	1.05	21	0.038
4	2	60	1.05	22	0.037
6	2	60	1.05	13	0.055
8	2	60	1.05	10	0.073
10	2	60	1.05	9	0.092
12	2	60	1.05	7	0.110
14	2	60	1.05	6.5	0.129
10	8	60	0	0.167	0.206
10	6.5	60	0	0.33	0.189
10	5	60	0	0.67	0.164
10	4	60	0	1.167	0.143
10	3	60	0	2	0.116
10	2	60	0	3.5	0.084
10	1	60	0	6.167	0.045
10	0.5	60	0	8.5	0.024
10	0.25	60	0	9.83	0.012

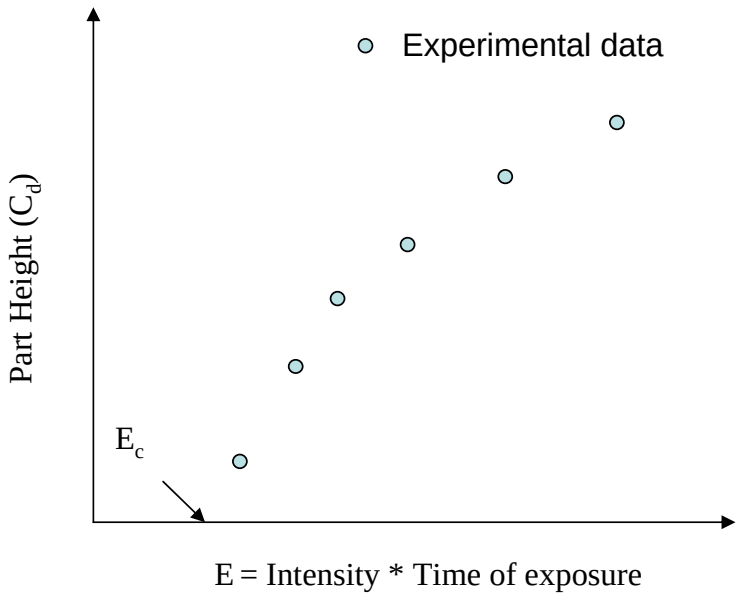

Figure 21: Schematic of typical working curve. A resin of fixed composition is exposed to UV light at a specific intensity and wavelength for varying periods of time. The parameters, E_c, and D_p, are matched to the experimental data to obtain a fit that applies for that specific resin composition and light intensity.

Here, C_d is the resulting cure depth (part height), D_p is the penetration depth of the light into the sample, E_c is the critical energy required before any cure is observed, and E is the energy of the light source [17]. By fitting E_c and D_p to working curve data, as shown schematically in Figure 21, the E_c–D_p model is capable of predicting part thickness very precisely. However, as can be seen from Equation (46), the parameters in the E_c–D_p model are not a function of the polymerization kinetics. Therefore, the E_c–D_p model is not adaptable to changes in intensity or resin composition. In order to determine optimal resin formulations without generating many such working curves to obtain new parameters, it is necessary for a model to include reaction kinetics. One example of an E_c–D_p model based on resin composition and kinetics, was a model proposed by Lee *et al.* [17]. This model is similar in form to Equation (46), but they compute the values of E_c and D_p using the reaction rate constants and intensity parameters. Using the variables and notations pertinent to our system in Equations (47)–(54), a similar relationship is derived here [17]. Recall from Equation (27) in

Chapter 2, the steady state analysis of radical concentration was used to arrive at the important quantity $k_p/\sqrt{k_t}$ in terms of initiation and monomer concentration. Equation (27) is integrated here, to the final monomer concentration at time t, to obtain:

$$ln\left(\frac{[M]_0}{[M]}\right) = \frac{k_p}{\sqrt{k_t}}\sqrt{k_d[In]}\,t \tag{47}$$

Recognizing that $\frac{[M]_0}{[M]}$ can be written in terms of conversion, given in Equation (28), with the variable α substituted for conversion, Equation (47) can be rearranged as follows:

$$ln\left(\frac{1}{1-\alpha}\right) = \frac{k_p}{\sqrt{k_t}}\sqrt{k_d[In]}\,t \tag{48}$$

Assuming that the critical conversion, α_c, yields a critical cure depth, z_c, the initial rate of initiation, R_i, can be substituted for the term inside the square root in Equation (48) to get a direct relationship between R_i and the time of cure for a specific α_c and $k_p/\sqrt{k_t}$. This inter-dependence of R_i and time of cure is plotted in Figure 22.

$$-ln(1-\alpha_c) = \frac{k_p}{\sqrt{k_t}}\sqrt{\frac{R_i}{2}}\,t \tag{49}$$

Plugging in the full form of R_i from Equation (20) into Equation (49),

$$-ln(1-\alpha_c) = \frac{k_p}{\sqrt{k_t}}\sqrt{2.3\phi\epsilon I_0 e^{(-2.3\epsilon[In]z_c)}\left(\frac{\lambda}{N_A\,h\,c}\right)[In]}\,t \tag{50}$$

The cure depth z_c or C_d as corresponding to Equation (46), in Equation (50) can be rearranged to obtain,

$$z_c = ln\left[2.3\phi\epsilon I_0\left(\frac{\lambda}{N_A\,h\,c}\right)\left(\frac{t\,k_p/\sqrt{k_t}}{-ln(1-\alpha_c)}\right)^2\right]\left(\frac{1}{2.3\epsilon[In]}\right) \tag{51}$$

Defining E as the maximum energy delivered per area, which is the incident energy,

$$E = I_0 t \tag{52}$$

D_p from Equation (46) can be described in terms of the parameters related to the initiator.

$$D_p = \frac{1}{2.3\epsilon[In]} \tag{53}$$

The rest of the terms inside the logarithm are combined into E_c from Equation (46).

$$E_c = \left(\frac{2.3\phi\epsilon\, N_A\, h\, c}{\lambda\, t}\right)\left(\frac{-ln(1-\alpha_c)}{k_p/\sqrt{k_t}}\right)^2 \tag{54}$$

A unit analysis on the above relationships for C_d, E, D_p and E_c shows that C_d and D_p have units of length, while E and E_c have units of energy per time. Thus, the above derivation provides a correlation between the kinetics of the reaction and the resulting cure depth. However, it is important to note that this analysis is based on the assumption that the radical concentration is at steady state. At the early stages of reaction, before the onset of gelation, the radical concentration cannot be expected to reach a steady concentration. In addition, the kinetics pertaining to oxygen inhibition cannot be included in the steady state analysis. Due to both these limitations, the gel time predicted by the steady state model does not match the deoxygenated or oxygenated microrheology data as seen in Figure 22.

Although the steady state model fails to make satisfactory part height predictions a critical conversion value can still be identified to determine the cure depth by using the double bond conversion predictions from the ODE model. The rate constants suitable for use with the ODE model were estimated in Chapter 3, and they are used here to fit the degree of conversion required to match the gel time values and part height values listed in Table 4. To do this, the ODEs in Equations (11)–(15), and Equation (39), were used to predict the conversion profile in several layers of a 120 micron deep vat (based on the spacer used in the microrheology experiments), as shown in Figure 23. Oxygen diffusion in the vertical dimension was included in the simulation by dividing the vat into slices, and allowing transfer of oxygen between the layers. Thus, each one of the layers had a different conversion and oxygen concentration. In Chapter 3, when rate constants were being estimated by fitting to the FTIR data, the conversion over all the layers was averaged and dark reactions were included in the "ex-situ simulations". In contrast, the gel time from microrheology records the time at the instant gelation starts to occur. Therefore,

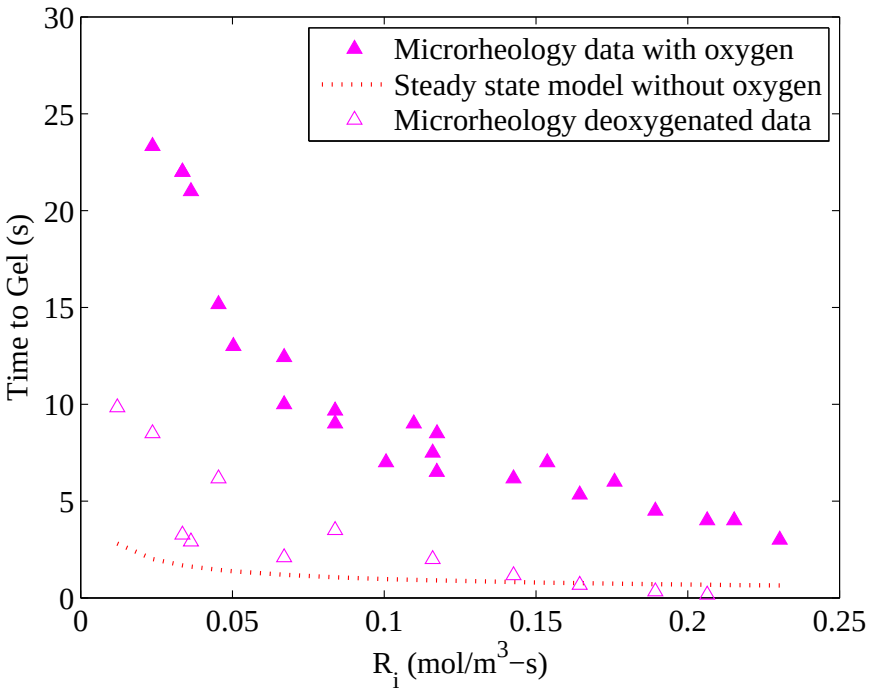

Figure 22: Steady state model results for TMPTA using the $k_p/\sqrt{k_t}$ of 0.4146 determined in Chapter 3 and $\alpha_c = 12\%$. The steady state model does not include oxygen inhibition, and it fails to predict conversion before gelation.

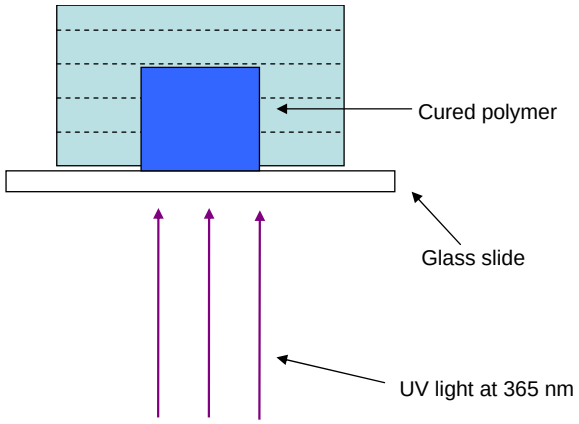

Figure 23: Schematic of the cure setup used in the experiments and the simulations.

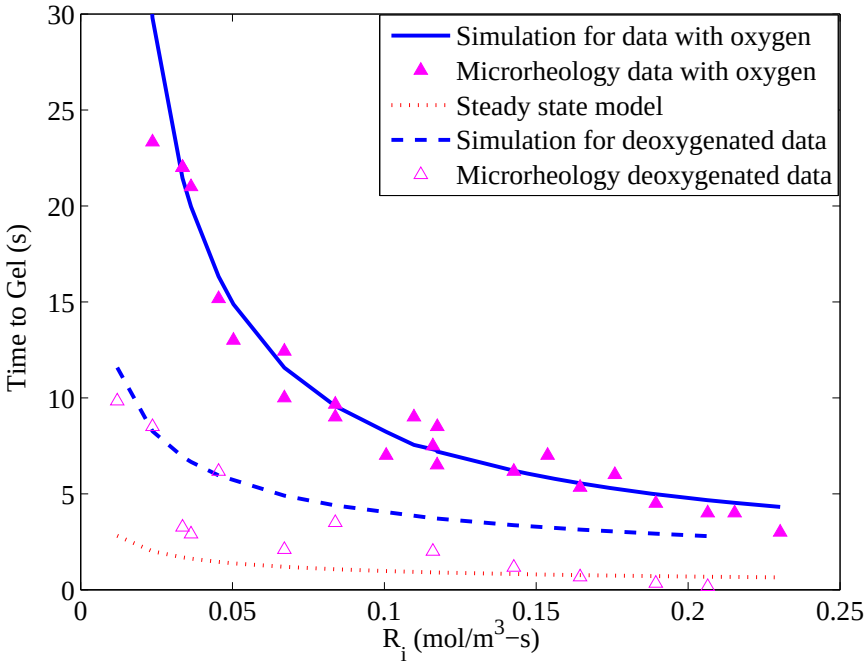

Figure 24: Estimating conversion cut-off from fit to microrheology data. Using the $k_p/\sqrt{k_t}$ of 0.4146, $k_p = 0.26\ m^3/mol\text{-}s$, $k_t = 0.39\ m^3/mol\text{-}s$ and $k_{toxy} = 2\ m^3/mol\text{-}s$ determined in Chapter 3 for TMPTA, a 12% conversion cut-off was determined by fitting to the microrheology data of TMPTA with oxygen.

dark reactions are not included in the simulations here. Also, the simulation results from all the layers are not averaged, since the data corresponds to cure at the depth that the microscope is focused on. Lastly, the simulated vat was divided into 24 layers of 5 microns each, and further discretization did not yield a significant difference in the results.

Using the R_i values for oxygenated TMPTA in Table 4, the critical conversion cut-off value was varied in the simulations to fit to the experimental gel time, T_{gel}, while using the rate constants from the fit to the FTIR data. When fitting the conversion cut-off value to match the microrheology data, the criterion was to find a single cut-off value that matches gel times of the entire data set. In this process it was determined that the T_{gel} values less than 1 second required matching conversion cut-off values which were too low to match the remaining gel time data. The fast

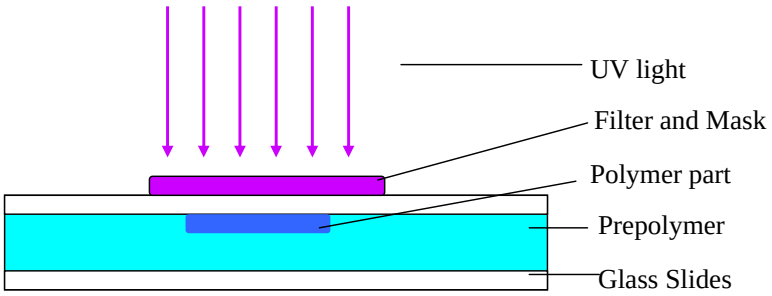

Figure 25: Schematic of blanket cure experiments in the presence of O_2.

kinetics at these high regimes might lead to a significant change in the value of R_i from time zero to the time of cure. Therefore, the deoxygenated microrheology data set was excluded when fitting the conversion cut-off value to the microrheology data. A further analysis of this data with blanket cure experiments is provided in Section 4.3. The resulting double bond conversion cut-off obtained from fitting to the microrheology data of TMPTA with oxygen, was 12%, while Flory's theory suggests a double bond conversion cut-off value of 20% for triacrylates (Table 3) [7]. In comparison to other acrylate systems, the conversion cut-off obtained from the fit to microrheology data is realistic. Tang *et al.* described a double bond conversion cut-off of 9% for tetracrylates. However, Flory's theory suggested a 14% double bond conversion cut-off for tetraacrylates (Table 3) [7]. This disparity led to the conclusion that an infinite network is not necessary to form a solid part [28]. Increasing the conversion cut-off value in the ODE simulations caused the simulated T_{gel} to increase. In addition, the fit was comparitively worse in the lower R_i regions because the T_{gel} increase was more significant there. However, the simulation results, shown in Figure 24 with 12% double bond conversion cut-off match the oxygenated data very well for the full range of R_i values.

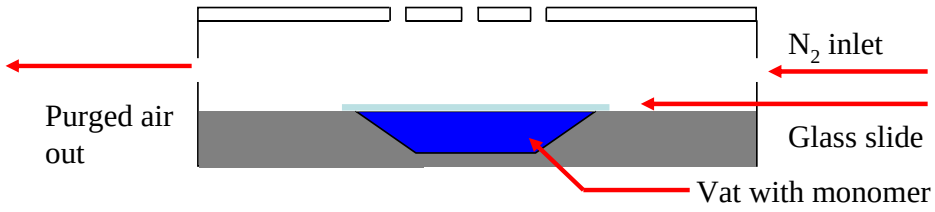

Figure 26: Schematic of nitrogen purging setup. The tight fitting lid has recesses that can be opened for curing after deoxygenation.

4.3 Correlation between cure depth from microrheology and part height

We conducted blanket cure experiments using the gel time from microrheology as the time of exposure, in order to confirm some of the deoxygenated data points shown in Figure 24 and also to correlate the cure depth from microrheology to a solid part height. In order to explain the poor fit between the simulation and experimental data for the deoxygenated TMPTA shown in Figure 24, nitrogen purged TMPTA samples were cured at several of the conditions listed in Table 4, and the results are shown in Table 5. The setup consisted of a nitrogen gas purging chamber with a vat to contain TMPTA as shown in Figure 26. Nitrogen gas flowed through the head space above the vat, and, over time, drove the oxygen out of the monomer. The vat containing TMPTA was purged for three hours before curing the sample in the experiments described here.

After we followed the above purging procedure, and cured for the desired exposure time, the glass slides resting on the surface of the monomer pool were pulled off, and a jet of air was used to remove any monomer from the surface of the solid part. The part was rinsed with isopropanol and dried with compressed air, just before being measured with a TalySurf Profilometer. A sample of 8 wt% TMPTA deoxygenated in the above fashion was cured for 0.2 seconds to mimic the data set in Row 27 of Table 4, but there was no observed cure. To confirm that this was not due to

Table 5: Cure height from blanket cure experiments.

I_0 (W/m^2)	$[In]$ wt%	$[O_2]$ (mol/m^3)	Cure time (s)	Cure height (μm)
10	0.25	60	0	9.83
10	5	1.05	9	113
10	5	1.05	8	98
10	5	1.05	6	64
10	5	1.05	4	0
10	8	0	3.5	300
10	8	0	1	150
10	8	0	1	140
10	8	0	1	160
10	2	0	3.5	110
10	2	0	3.5	140

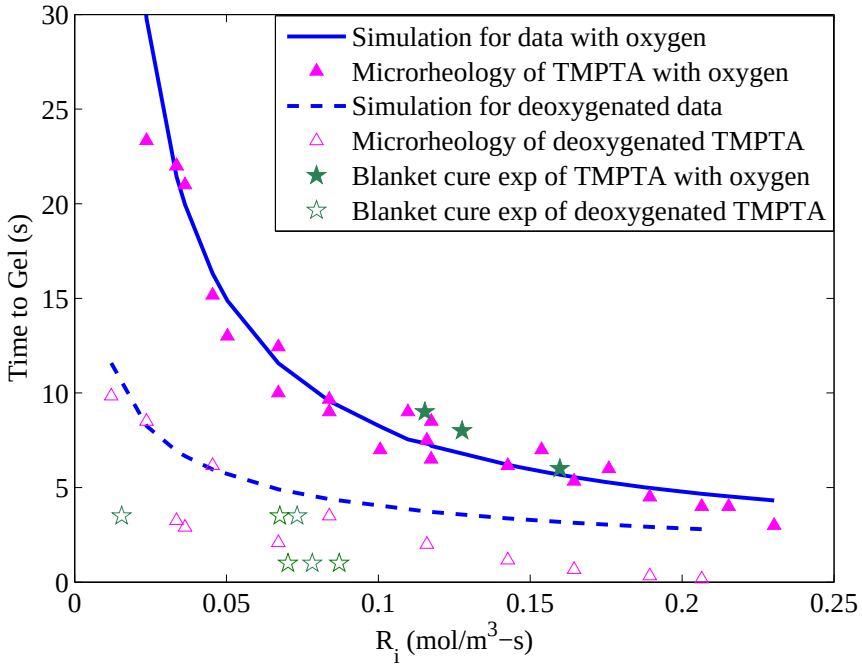

Figure 27: Blanket cure experimental data of TMPTA is shown here in addition to microrheology data. The blanket cure data for TMPTA with oxygen shows a good match to the microrheology data. However, the part height from the deoxygenated blanket cure experiments was thicker than expected from the deoxygenated microrheology data set. Blanket cure experiments of deoxygenated TMPTA were also conducted for higher R_i values, but there was no observed cure.

insufficient deoxygenation, another initial condition from Table 4 on row 32, with 2 wt% initiator solution of TMPTA was exposed to the gel time of 3.5 seconds. The resulting part height was not 60 microns, but 110 microns. This high part height result suggested that the energy dose was sufficient to cure to the instantaneous cure depth, shown in Table 4, and also led to possible additional solidification from dark reactions. However, if the vat was not sufficiently deoxygenated, the oxygen inhibition reactions would take precedence over propagation due to dark reactions. This lack of oxygen inhibition reactions suggests that the deoxygenation method was thorough, but some of the exposure times listed in Table 4 did not yield a solid part because the required critical energy was not supplied. The deoxygenated sample undergoes rapid reaction and is susceptible to significant changes in part height from minor fluctuations, as seen in Table 5, therefore, R_i alone may not be sufficient to capture the reaction behavior of the deoxygenated data set. Thus, the deoxygenated data set was disregarded in determining the conversion cut-off, and the discrepancy between the model prediction and deoxygenated experimental data is observable in Figure 27.

The elaborate setup required for the deoxygenated experiments was not necessary for the experiments with TMPTA with oxygen. Instead, two glass slides with a 1 mm glass spacer were used to hold the sample as shown in Figure 25. Then, a solution of 5 wt% DMPA in TMPTA was pipetted into the space between the slides. Experiments were run to encompass the initial conditions shown in rows 1-5 of Table 4, and the results are shown in Table 5. All the samples were exposed to light at 10 W/m^2, for different exposure times. After exposure, the excess monomer was poured out and a nitrogen gun was used to remove any monomer from the surface of the solid part. Just before measurement with a TalySurf profilometer, the part was rinsed with isopropanol and dried with compressed air, as in the case with deoxygenated samples.

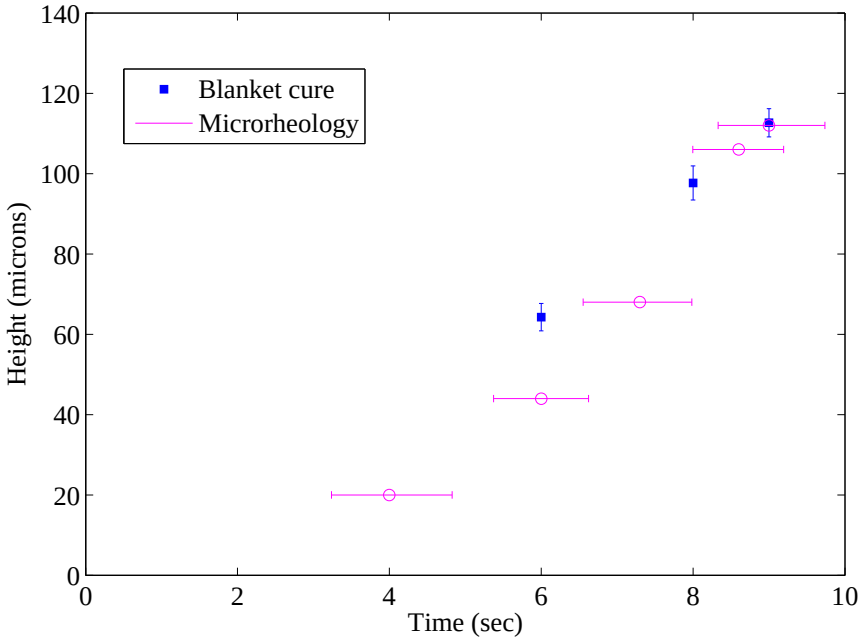

Figure 28: Comparison between part height from microrheology and blanket cure. 5 wt% DMPA in TMPTA cured with intensity of 10 W/m^2 at 365 nm.

The comparison between the part height from blanket cure experiments and microrheology experiments is shown in Figure 28. Although there was a lack of agreement, in the deoxygenated case, between part height from blanket cure and cure depth from microrheology , the one-to-one correlation between the data from the two types of experiments, in the case when oxygen is present, is consistent. The measured part height from the blanket cure experiments shows us that part height is measured accurately with microrheology, at least above 60 μm. This implies that the conversion cut-off obtained from the fit to microrheology data can be used to make part height predictions for blanket cure experiments. The rate of initiation, R_i, was necessary in order to combine all the variables that impact gel time, and part height, when characterizing the oxygenated TMPTA data. However, the fast kinetics of deoxygenated TMPTA seem to involve other factors that are not incorporated into R_i. In the scope of this project, systems with oxygen are of more interest because deoxygenation of the sample before cure would be an additional step in the process. Furthermore,

additional modifications would have to be implemented to ensure that no oxygen enters the system during the cure. Yet another added benefit of having oxygen in the sample, is that it acts as a natural inhibitor, and provides greater control over the resulting part height. As observed from repeated experiments using deoxygenated TMPTA, even random fluctuations in the cure environment can lead to significant difference in the resulting part height. Using the double bond conversion cut-off of 12% from this chapter, and rate constants from Chapter 3, part height predictions can be made for oxygenated TMPTA samples. Chapter 5 has further discussion regarding the factors that impact part height, and also part height predictions from a joint fit to the aforementioned experimental data.

CHAPTER V

PART HEIGHT PREDICTIONS WITH THE KINETIC MODEL

5.1 Effect of initiator concentration, intensity and exposure time

The rate constants and conversion cut-off value for TMPTA from Chapters 3 and 4 provide the necessary parameters for predicting part height. Figures 29 and 30 are plots of part height as a function of energy dose and initiator concentration for a system without and with oxygen, respectively. A similar plot was shown by Lee *et al.* for a deoxygenated system using the steady state model [17]. However, since the steady state assumption was shown to be inapplicable to the scope of this project in Section 4.2, the effects of energy dose and initiator concentration on part height are examined through use of the ODE model developed in the previous chapters.

Figures 29 and 30 show reaction simulations of TMPTA with initiator concentrations in the range of 0.25-8 wt%. The varying energy doses shown are the product of the incident intensity of 10 W/m^2 and different exposure times, based on the equation for energy dose provided in Equation 52. These settings represent the values in Rows 7–15 of Table 4. The rate constants in $m^3/mol\text{-}s$ used in these simulations are k_p of 0.26, k_t of 0.39 and k_{toxy} of 2. For each energy dose in Figures 29 and 30, as the initiator concentration is increased, the part height does not continually increase. Instead, there is a clear optimum concentration of initiator for each energy dose that will produce the thickest part. This is a trend that the E_c–D_p model cannot provide without experimental data for each one of the experimental conditions.

The separate influence of the components of energy dose, namely the intensity and

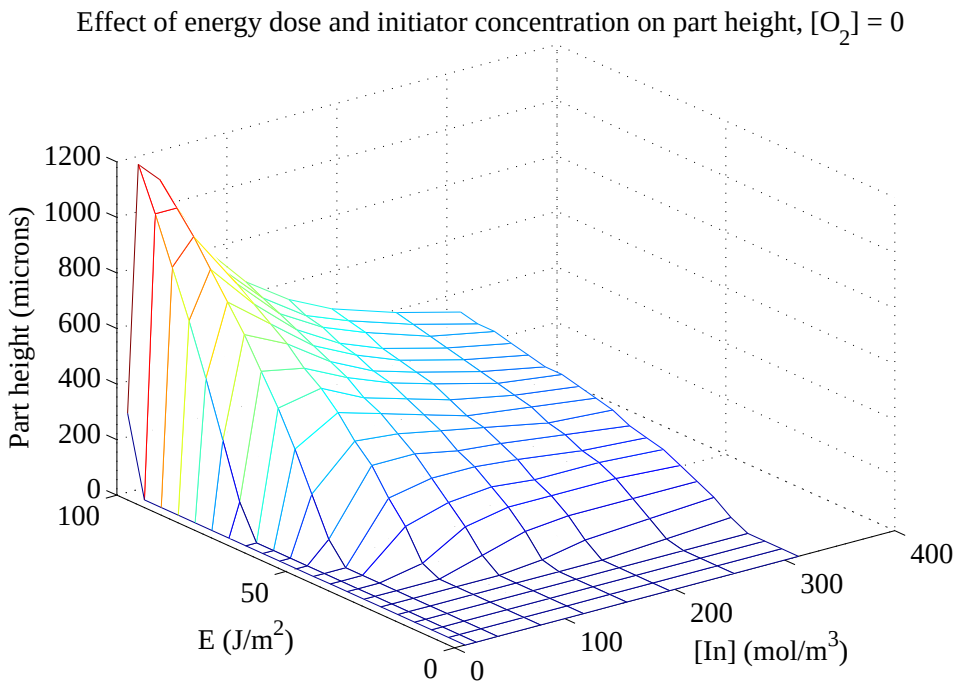

Figure 29: Effect of energy dose and initiator concentration on deoxygenated TMPTA. Rate constants from Row 3 of Table 2 and conversion cut-off = 12%.

exposure time is explored in Figures 32 and 33. In Figure 32 the simulated exposure time is changed for each intensity so that the total value for energy is always equal to 100 J/m^2. Although the energy delivered is the same for all the points in Figure 32, the resulting part height values for each combination of intensity and exposure time are different. Figure 33 contains experimental blanket cure data that have all been exposed to the same energy dose of 100 J/m^2, with different intensity and cure times. Curing at low intensity, for a long time yields a thicker part height than curing at high intensity for a shorter exposure time. The part height increases again at the higher intensity values which might be due to the faster reaction conditions, and higher incidence of dark reactions. From Figures 32 and 33 it can be seen that E, which is central to the working curve plots used to fit the parameters E_c and D_p, is independently influenced by its components I_0 and exposure time. Looking at this from a mechanistic perspective, the reason for this behavior lies in the competing rates

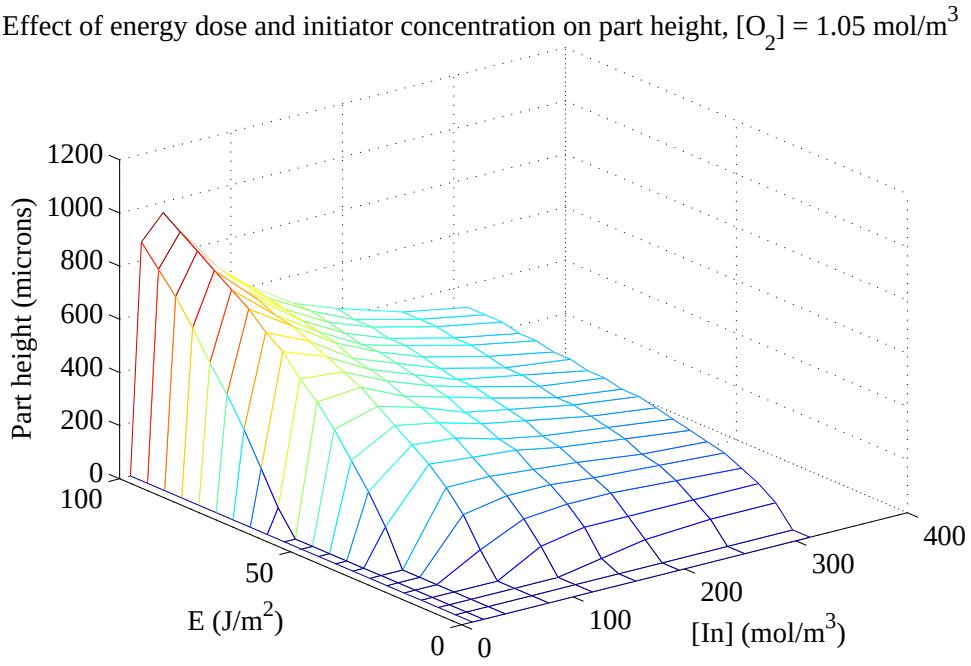

Figure 30: Effect of energy dose and initiator concentration on TMPTA with $[O_2]$= 1.05 mol/m^3. Rate constants from Row 3 of Table 2 and conversion cut-off = 12%. The final part height is lower here than in the deoxygenated case, but there is still an optimum initiator concentration for each energy level.

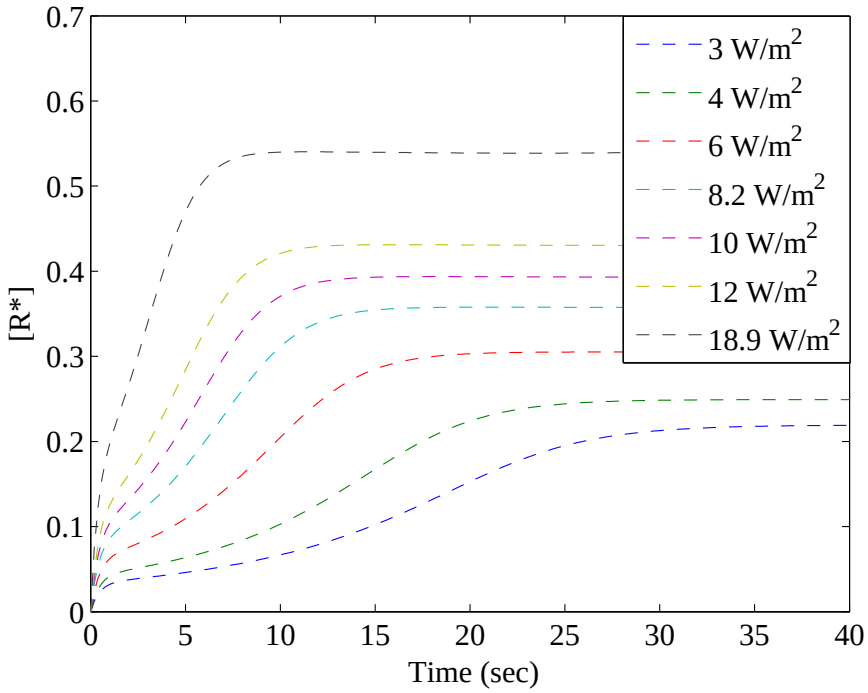

Figure 31: E= 100 J/m^2 for all the simulated curves shown here, and [In]=5 wt%. The corresponding exposure time for each of the intensities is calculated as t = $E/Intensity$. Although all of the simulations contain the same initiator concentration, and the energy dose is the same, the concentration of live radicals in the system is different. At lower intensities, there are fewer live radicals in the system, whereas at higher intensities, there are a more. This means that at the higher intensities, the probability of a termination reaction is increased, thus changing the resulting part height as seen in Figure 32.

of initiation, propagation and termination. When the rate of initiation is low due to lower intensity, the concentration of live radicals in the system at any given time will be lower. Thus the likelihood of these radicals propagating via reaction with double bonds is high. On the other hand, when the rate of initiation is high due to a higher intensity, there are more live radicals in the system and the likelihood of radical termination is increased. This can be seen from the plot of radical concentration versus time at various intensities in Figure 31.

Thus, the ODE model shown here, along with the rate constants and conversion cut-off from Chapters 3 and 4 captures the influence of intensity, exposure time, and initiator concentration on the resulting part height. Collectively, Figures 29–33 show

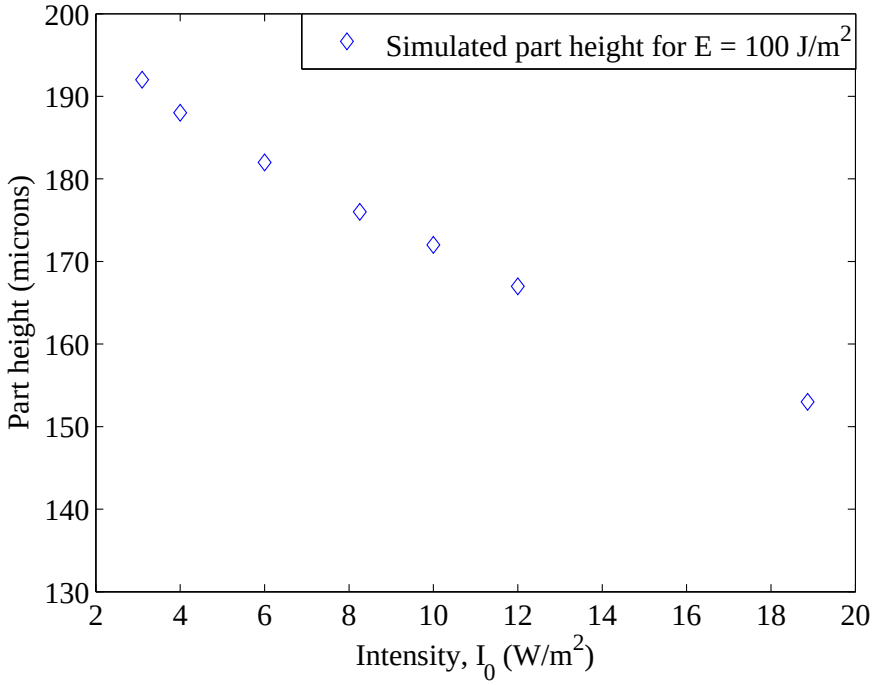

Figure 32: E= 100 J/m^2 for all the simulated points here. Exposure time, t = $E/Intensity$.

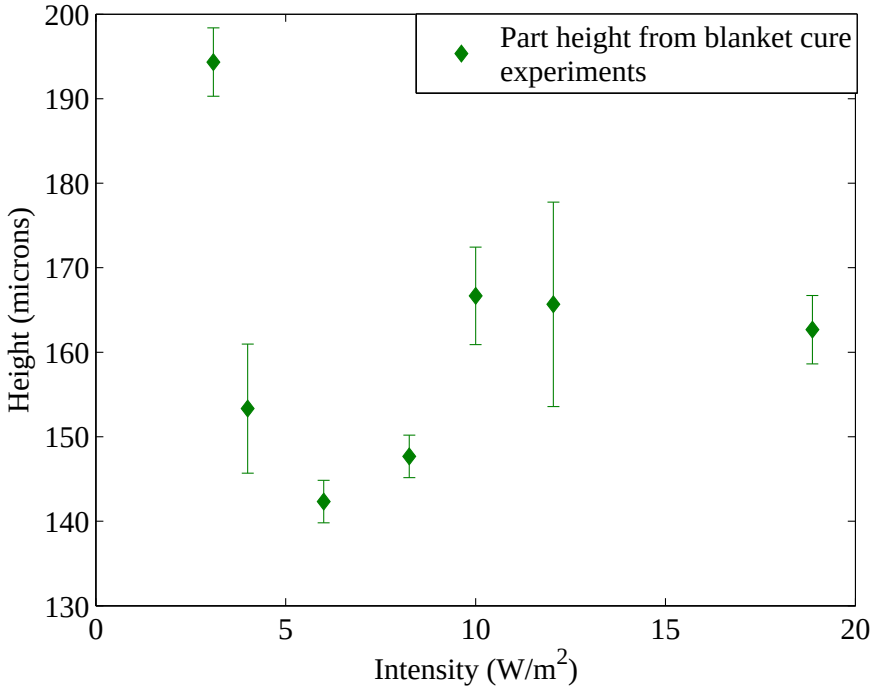

Figure 33: E= 100 J/m^2 for all the blanket cure data points shown here. Exposure time, t = $E/Intensity$.

why the E_c–D_p model, fit to data points from a single resin composition, cannot be used to predict part height across varying $[In]$ and I_0.

5.2 Simulated working curves from the ODE model and E_c–D_p model

So far, we have shown that the ODE model presented here accounts for the relevant reaction kinetics, and that it can be used as a tool for process planning to determine optimum resin formulations and appropriate light intensities to use. There is still a question remaining of whether this ODE model can make better part height predictions than the E_c–D_p model can. In E_c–D_p models, the parameters E_c and D_p are obtained by fitting to part height and energy dose experimental data. Accordingly, when E_c and D_p were fit to the data from Rows 1–6 of Table 4, all at I_0 of 10 W/m^2, and at 5 wt% DMPA, the resulting E_c value was 31 J/m^2 and D_p was 96.7 microns. However, since E_c–D_p models are usually intended to be fit to blanket cure experimental data, if E_c and D_p are fit to the blanket cure data in Figure 28, the E_c value increased to 39 J/m^2 and D_p increased to 138 microns. These E_c and D_p values were used to generate the simulated working curve, and the results are shown in Figure 34. Part height predictions for the same conditions were also generated using the ODE model, and those simulation results are also shown in Figure 34. As expected, the E_c–D_p model, which has been customized for these data points, fits the experimental data slightly better than the ODE model does. This is because the parameters used in the ODE model have been fit to the entire range of FTIR and microrheology data of TMPTA, rather than the selected blanket cure data shown here. For the data points shown here, the simulation from the ODE model underpredicts the time required to cure to the desired part height at higher thicknesses.

This suggests that the ODE model is more appropriate for selecting which initiator concentration levels or intensity to work with, but the E_c–D_p model is better at part height predictions once the particular resin composition has been chosen. Once the

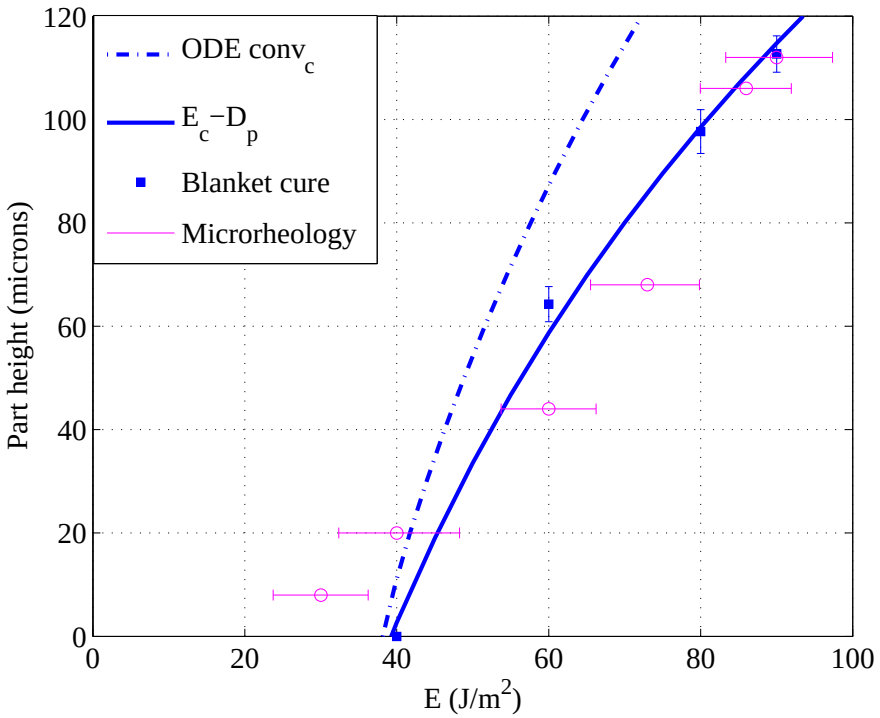

Figure 34: Part height prediction with both ODE model and E_c–D_p model. The ODE model uses the parameters from Chapters 3 and 4 with k_p= 0.26 $m^3/mol\text{-}s$, $k_p/\sqrt{k_t} = 0.4146$ and $conv_c = 12\%$.

process conditions are selected using the ODE model, a working curve should be constructed using experimental data points at the selected resin composition and intensity for varying exposure time points. E_c and D_p can be fit to this particular process, and these variables can then be used in subsequent part height predictions.

5.3 Can the fit from the ODE model be improved?

5.3.1 Fitting to different data sets together

Noting that the E_c–D_p model makes better final part predictions, one should ask whether the ODE model can be improved by fitting to the FTIR data and the selected microrheology data sets together or by fitting only to the blanket cure data in the same way that the E_c–D_p model is fit. In Section 5.2, part height predictions shown in Figure 34 were obtained using the rate constants from a fit to the FTIR data, and the conversion cut-off from fitting to all the oxygenated TMPTA microrheology data points separately. As shown in earlier chapters, the $k_p/\sqrt{k_t}$ was first obtained from the deoxygenated FTIR data and then the k_p, k_t and k_{toxy} were fit using that information. Instead of obtaining the parameters step-wise in this manner, in the joint fit, the k_p, k_t, k_{toxy} as well as the conversion cut-off were all varied in the optimization to jointly match data from FTIR and microrheology data from Rows 1–6 of Table 4. The new $k_p/\sqrt{k_t}$ of 0.4659 is slightly higher than the previous value of 0.4612, but the k_{toxy} is lowered to 1 $m^3/mol\text{-}s$. The lower value of k_{toxy} is lower due to the optimization trying to match the data sets from FTIR at the higher initiator concentrations of 5 and 10 wt%. The conversion cut-off value from the joint fit is 28%, which is higher than the theoretical α_c of 20% given in Chapter 4. Based on the discussion in Chapter 4, the conversion cut-off required to make a solid part should be lower than the theoretical value, and this is supported from the conclusions by Tang *et al.* as well [28]. Therefore, the higher conversion cut-off from the joint fit makes less sense physically. Overall, comparing the fit from the ODE model using

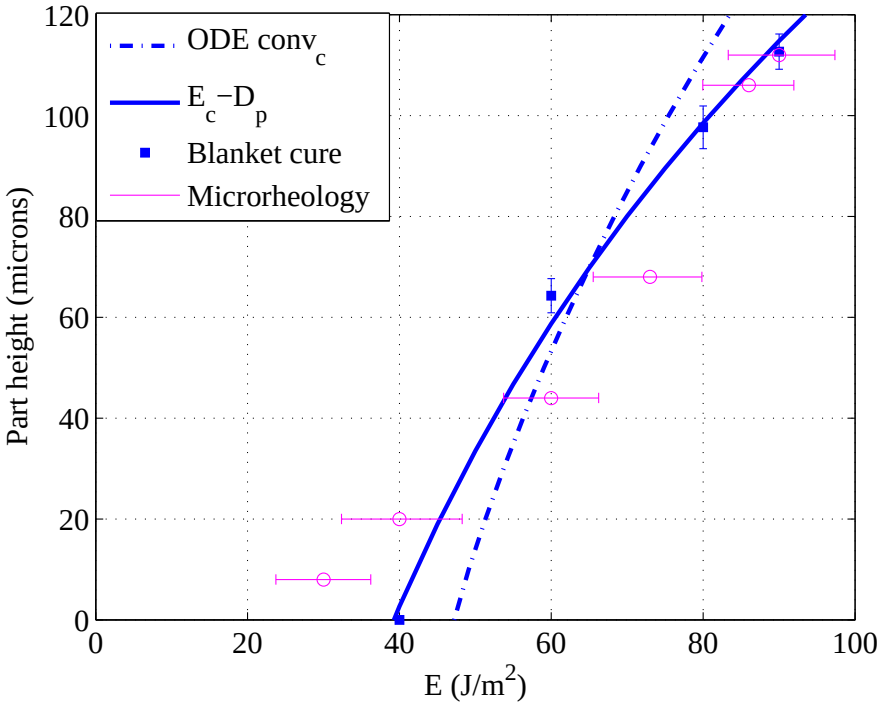

Figure 35: Part height prediction with both ODE model and E_c–D_p model. Here, the ODE model uses parameters from the joint fit to the IR data sets as well as the microrheology data in Rows 1–6 of Table 4.

parameters from the joint fit to the blanket cure data, the result in Figure 35 shows that there is only a slight improvement as compared to the results in Figure 34.

The new rate constants are better suited to match the data from the higher initiator concentrations in the ex-situ FTIR data, and this is evident from the lower RMSE value shown in Table 7. A comparison of Figure 39, (a) and (b), shows that in the case of the FTIR data with oxygen, the lag in the 0.5 wt% DMPA data set is slightly less pronounced in the joint fit due to the higher ratio of $k_p/\sqrt{k_t}$. The fit to the entire microrheology data set is still very good compared to the previous fit as seen in Figure 40. However, contrary to expectations, the conversion cut-off obtained from the joint fit is higher than the theoretical value, and this does not make sense physically. Therefore, although the joint fit matches both the data sets better overall, the parameters obtained from the earlier fit are more realistic.

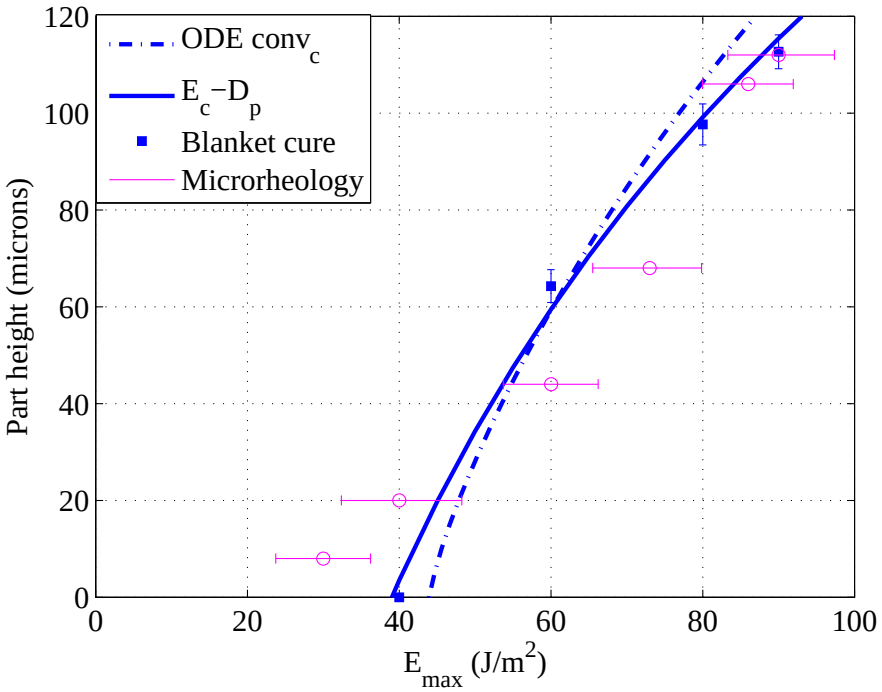

Figure 36: Part height prediction with both ODE model and E_c–D_p model using parameters fit to the blanket cure data. The part height predictions are noticeably better than the predictions in Figure 34 and Figure 35, but this comes at the cost of decreased versatility in the ODE model. The values of the parameters are as follows: $k_p = 0.26\ m^3/mol\text{-}s$, $k_t = 0.0013\ m^3/mol\text{-}s$, $k_{toxy} = 5.39\ m^3/mol\text{-}s$ and $conv_c = 8.2\%$. When these parameters are used to predict the double bond conversion and gel time, the corresponding RMSE values have increased as shown in Table 7.

If the parameters in the ODE model are fit to the blanket cure data directly, in the same way that the E_c–D_p model parameters are, the rate constants change to the values shown in Figure 36, while the conversion cut-off remains about the same. Figure 36 has the part height predictions with these new parameters, and the fit is greatly improved in comparison to the joint fit results in Figure 35. The corresponding RMSE values for predicted double bond conversion and gel time data are shown in Table 7 and the fit to the FTIR data and microrheology data has deteriorated. A comparison of Figure 39, (a) and (c) shows that the lag in the lowest initiator curve has increased in (c). Once the oxygen quenching phase is completed, the reaction proceeds very quickly. This is due to the $k_p/\sqrt{k_t}$ in Figure 39 (c) being much higher at 7.2. On the other hand, the $k_p/\sqrt{k_t}$ in Figure 39 (a) is only 0.4146. Figure 40 (a) and (c) show that the fit to the microrheology data with the parameters from fitting to blanket cure data alone is also not very good. Table 7 contains a quantitative comparison of the RMSE values using the parameters fit to the blanket cure data. The RMSE values confirm that the parameters from fitting to blanket cure data alone do not predict the conversion and gel time accurately. However, Figure 36 shows that if the parameters of the ODE model are fit to the blanket cure results for a specific cure recipe, then it is capable of making precise part height predictions just as the E_c–D_p model does. In contrast, the parameters obtained from a more mechanistic fit to the available double bond and microrheology data are capable of more versatile predictions and they will be able to make predictions in a wider range of cure recipes.

5.4 Effect of temperature on part height predictions

The rate constants described in earlier chapters did not include a dependence on the temperature of the reaction volume. As a final check on how the heat released during polymerization affects the rate of cure, an Arrhenius relationship was introduced to link the rate constants to the temperature in the simulation volume. This

section contains a quantitative description of the amount of heat generated during polymerization, the amount of temperature increase, and the associated effect of this temperature increase on the rate constants. the general heat balance equation used is shown in Equation 55.

$$\rho C_p \frac{dT}{dt} = k\frac{d^2T}{dz^2} + \Delta H_p R_p \tag{55}$$

$$k_p = k_{p0} exp\left(\frac{E_{Ap}}{R}\left(\frac{1}{T_0} - \frac{1}{T}\right)\right) \tag{56}$$

$$k_t = k_{t0} exp\left(\frac{E_{At}}{R}\left(\frac{1}{T_0} - \frac{1}{T}\right)\right) \tag{57}$$

Table 6 contains a description of the parameters used here and their values. The Arrhenius dependence of the rate constants is shown in Equations (56) and (57). The reaction volume was divided into slices in one dimension again, as in Figure 23, and the volume inside each slice was assumed to be well-mixed. In order to ensure that this assumption holds true, the thermal diffusion length for the fastest reaction time of 0.5 seconds was calculated to be 7 microns, using the thermal conductivity listed above. Thus, slices of 5 microns were chosen to make sure there was sufficient mixing. Heat transfer was allowed between adjacent slices, and the thermal conductivity parameter determined the rate of heat flux.

Table 6: The above parameters values were used in determining the temperature increase in the reaction volume.

Parameter	Description	Value	Units	Source
ρ	Density	1.018	g/cc	Sartomer
C_p	Heat capacity	1.7	$J/g\text{-}K$	[15]
k	Thermal conductivity	0.123	$W/m\text{-}K$	[15]
ΔH_p	Heat of polymerization	2.58e5	J/mol	[15]
E_{Ap}	Activation energy for k_p	1627	$J/mol\text{-}K$	[28]
E_{At}	Activation energy for k_t	2103	$J/mol\text{-}K$	[28]
T_0	Initial temperature	298	K	–
R	Gas constant	8.314	$J/mol\text{-}K$	–
k_{p0}	Value at 298 K	0.26	$m^3/mol\text{-}s$	Chapter 3
k_{t0}	Value at 298 K	0.39	$m^3/mol\text{-}s$	Chapter 3

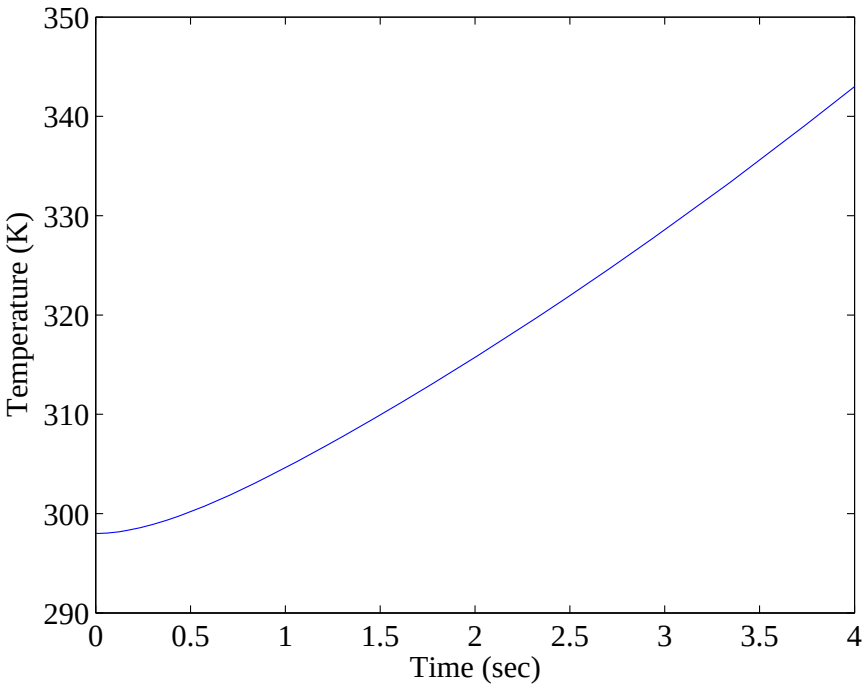

Figure 37: Temperature change in a simulated volume of 5 wt % DMPA with oxygen, being cured for 4 seconds. The top and bottom slides at the boundaries are assumed to be at room temperature.

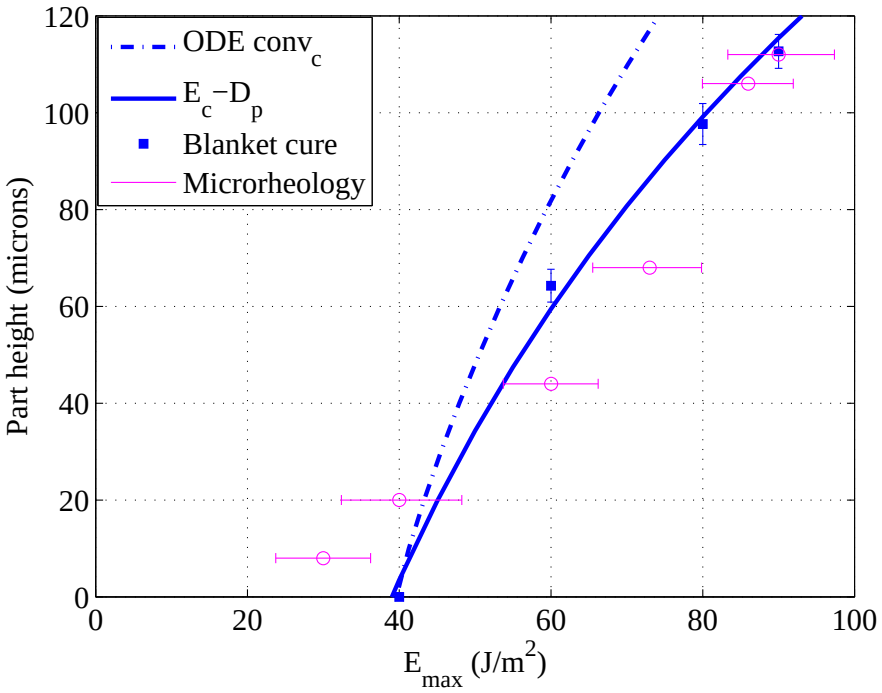

Figure 38: Part height predictions with rate constants that depend on the temperature of the reaction volume.

A sample temperature profile is shown in Figure 37 for a system of 5 wt % DMPA, incident intensity of 10 W/m^2 and cure time of 5 seconds. The rate constants did not increase much for the range of temperature increase shown here, and the impact on the simulated double bond conversion or gel time was very minimal. Table 7 contains the RMSE values when comparing FTIR experimental data to simulated double bond conversion data generated by using the temperature dependent rate constants. It also contains the RMSE values when comparing microrheology data to simulated gel time data generated using the temperature dependent rate constants. Figure 38 contains the comparison of predicted part height to experimental blanket cure data while using the temperature dependent parameters. There is no difference in the predicted part heights in Figures 34 which uses the original parameters fit separately to all the data sets, and Figure 38 which uses the parameters that are influenced by temperature.

Table 7: Comparison of blanket cure fit parameters and joint fit parameters fit from joint fit parameters to parameters from Chapters 3 and 4. Estimated rate constants from all three data sets shown above.

Fit type	Separate	Joint	Blanket cure	Temperature
TMPTA with O_2	21.28	16.56	57.2	21.28
Microrheology Rows 1–6 of Table 4	0.58	0.66	0.33	0.52

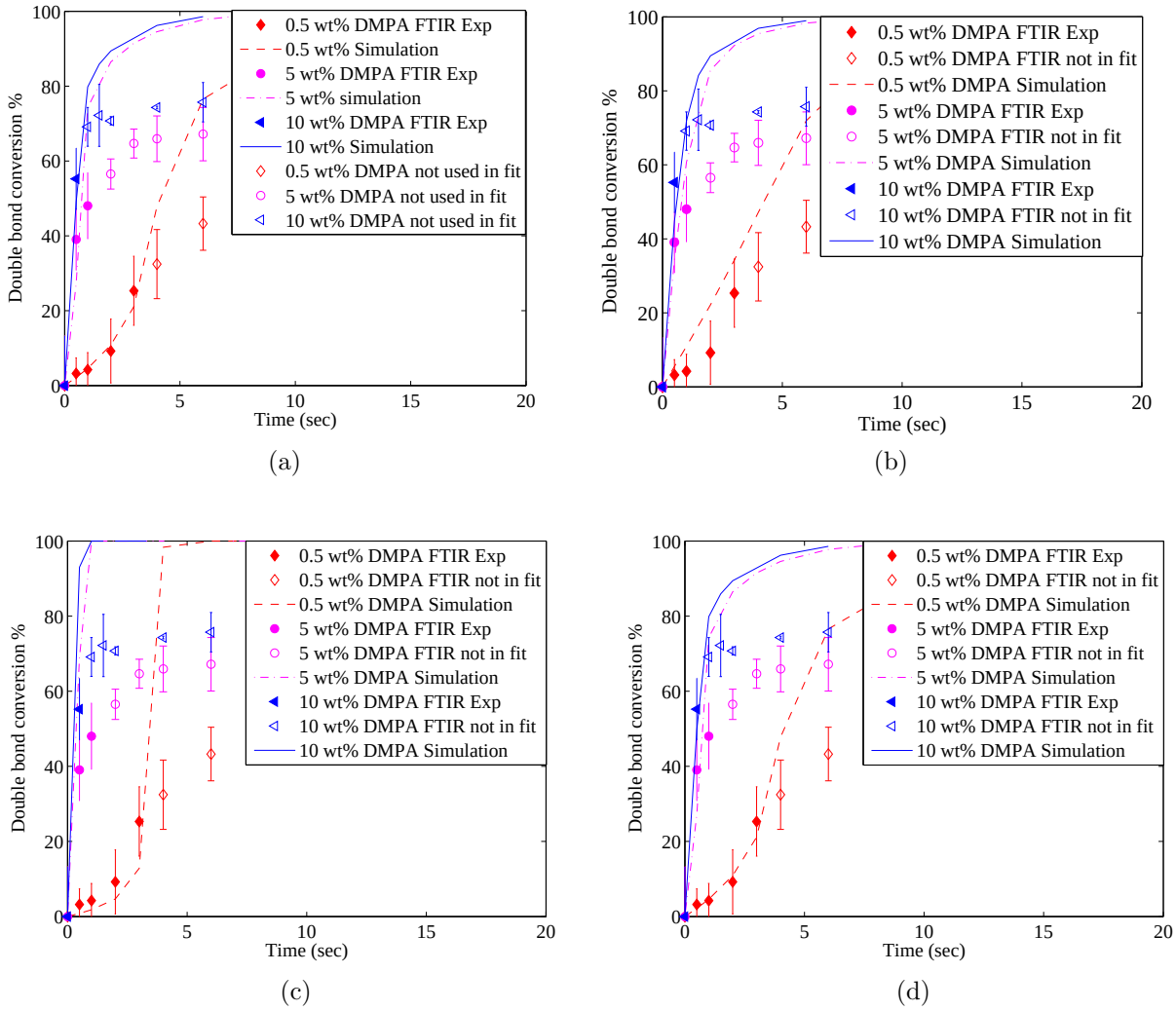

Figure 39: Comparison of TMPTA parameters. (a) Simulation results from estimated rate constants in Chapter 3. $k_p = 0.26\, m^3/mol\text{-}s$, $k_{toxy} = 2\, m^3/mol\text{-}s$, and $k_p/\sqrt{k_t} = 0.4146\ (m^3/mol\text{-}s)^{0.5}$. (b) The lag in the simulation is reduced due to the lower $k_{toxy} = 1 m^3/mol\text{-}s$. The joint fit $k_p/\sqrt{k_t}$ is 0.4659 $(m^3/mol\text{-}s)^{0.5}$ and $k_p = 0.26 m^3/mol\text{-}s$. (c) Simulation using parameters from fit to blanket cure data only. $k_p = 0.26\ m^3/mol\text{-}s$, $k_t = 0.0013\ m^3/mol\text{-}s$, $k_{toxy} = 5.39\ m^3/mol\text{-}s$ and $conv_c = 8.2\%$. (d) Simulation using rate constants that have an Arrhenius dependence on temperature of the system.

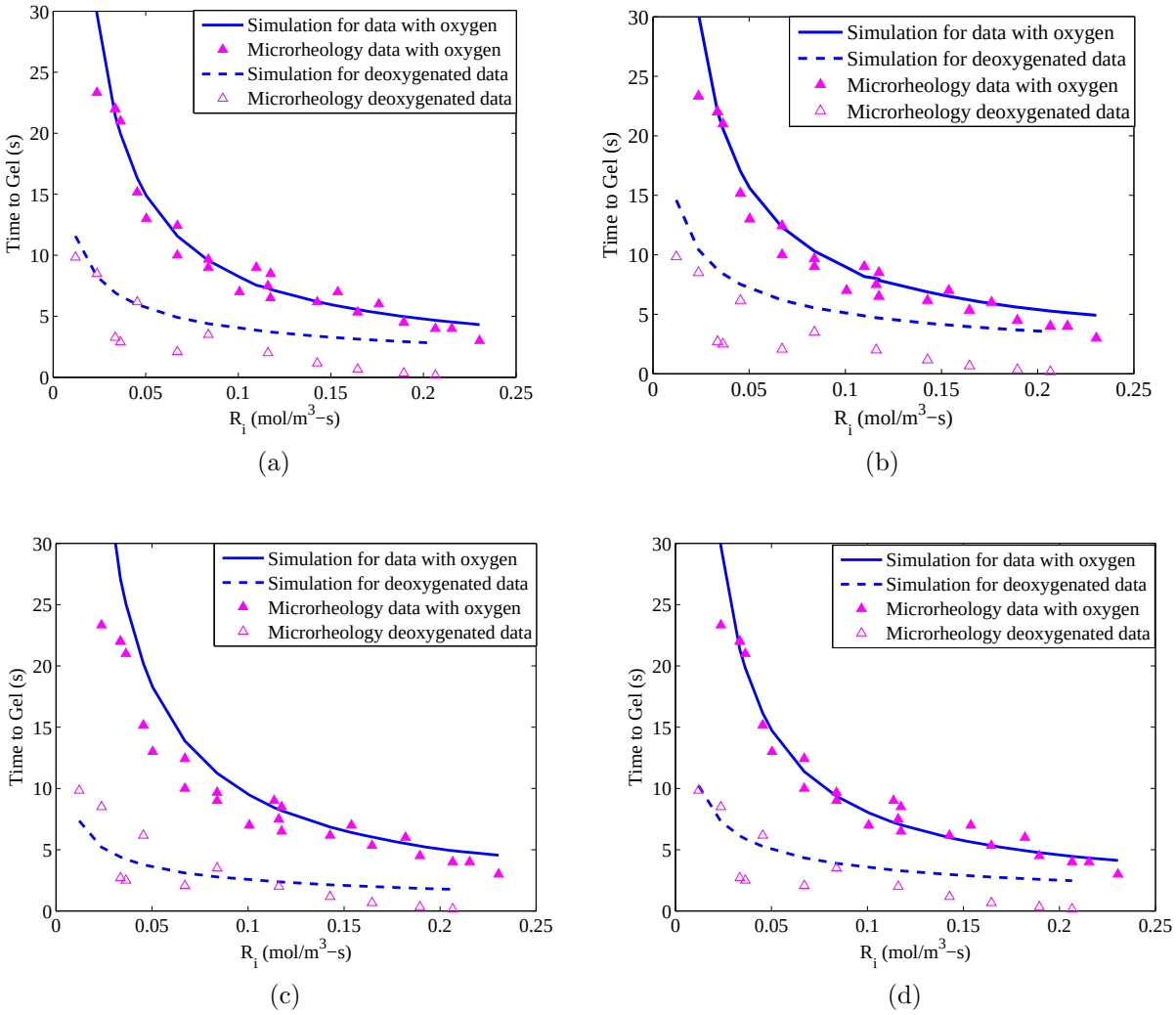

Figure 40: Comparison of simulations to match microrheology data. (a) Fit to microrheology data shown in Chapter 4, $k_p = 0.26\ m^3/mol\text{-}s$, $k_{toxy} = 2\ m^3/mol\text{-}s$, $k_p/\sqrt{k_t} = 0.4146\ (m^3/mol\text{-}s)^{0.5}$ and $conv_c = 12\%$. (b) Simulation using joint fit parameters, $k_p = 0.26\ m^3/mol\text{-}s$, $k_p/\sqrt{k_t} = 0.4659\ (m^3/mol\text{-}s)^{0.5}$, $k_{toxy} = 1\ m^3/mol\text{-}s$ and $conv_c = 28\%$. (c) Simulation using parameters from fit to blanket cure data only. $k_p = 0.26\ m^3/mol\text{-}s$, $k_t = 0.0013\ m^3/mol\text{-}s$, $k_{toxy} = 5.39\ m^3/mol\text{-}s$ and $conv_c = 8.2\%$. (d) Simulation using rate constants that have an Arrhenius dependence on temperature of the system.

CHAPTER VI

CONCLUSION

The aim of this project was to create a model that would be useful in process planning for stereolithography applications. The need for this versatile model arose from the limitations of currently used E_c–D_p models which make very precise part height predictions, but cannot be used to determine the most effective resin composition and intensity, collectively known as the cure recipe. Each cure recipe has a unique E_c and D_p fit, which is determined by fitting to experimental data. However, when there is a question regarding which cure recipe is ideal, running experiments at multiple cure recipes is inefficient.

The ODE model presented here is a solution to this limitation, as it is capable of predicting part height as a function of all the variables that impact cure. The rate constants necessary for this model were estimated by fitting to conversion data from FTIR of TMPTA with and without oxygen. At the onset of the project, molecular weight was proposed as a more accurate predictor of part height, but given the data available currently, conversion appears to be sufficient. In future studies, the KMC model is a viable method to predict molecular weight, and a few simulations predicting molecular weight evolution during the reaction are shown in Chapter 3.

The critical conversion value, to indicate that the polymer has cured, was estimated by fitting to gel time data from microrheology. In order to justify the use of gel time data from microrheology to estimate the critical conversion value, we examined the correlation between part height and gel point. This resulted in three key outcomes. First, the initial rate of initiation, R_i, combines all the parameters that

impact part height for oxygenated TMPTA, but R_i alone is insufficient when predicting the rapid cure and onset of gel in deoxygenated TMPTA. Second, deoxygenated data is not suitable for use in processes where accurate part height needs to be made because the lack of inhibition leads to rapid reaction, and minor fluctuations in composition result in large changes in height. Third, the blanket cure data, of TMPTA with oxygen, matched the microrheology data, which justified the use of the extensive microrheology data to determine the conversion cut-off.

In the process of determining a critical conversion value, we showed that a steady state model is insufficient to predict part height for the deoxygenated case. The assumption that the radical concentration is at steady state fails in the early conversion regime, before the onset of gel, which is the region of interest here. In addition, the steady state model is not applicable to systems with oxygen because the analytical solution does not incorporate oxygen inhibition kinetics, and therefore cannot predict the inhibition lag time. Thus, correlating E_c and D_p to kinetic parameters through the steady state assumption does not yield accurate part height predictions.

Although it was already known that E_c and D_p models are specific to each cure recipe, we further showed why a working curve, which is the basis for E_c–D_p models, is not adaptable to changes in cure recipe without experimental data at the new conditions. For instance, when the same energy was delivered through combinations of different intensities and exposure time, the resulting part heights were different. Specifically, having a higher intensity, with a shorter exposure time resulted in smaller part height. This was shown to be due to the competing effects of propagation and termination which depended on the rate of radical generation. Similarly, when intensity and exposure time were held constant, increasing initiator concentration showed that there is an optimum concentration for each energy dose that yields the thickest part height. This initiator concentration is not necessarily the highest concentration, and this is due to the loss of light to initiator molecules. The benefit

of having more initiators, and therefore more radical generation is outweighed by loss of intensity due to absorbance by the initiator molecules at a critical point. This is an important process behavior that the process designer should be aware of, so that both the initiator and energy are used efficiently.

The final ODE model which incorporates oxygen diffusion and attenuation of intensity with cure depth is a versatile model that is a function of factors such as cure depth, z, incident intensity, I_0, and initiator concentration, $[In]$. This model is useful when deciding which combination of settings is best suited for the desired product. Once the process parameters are decided upon, it can be used in the same way that the E_c–D_p model has been used, to make part height predictions. Although the model predictions shown in this thesis are mostly related to one dimensional variations in oxygen concentration and temperature, the model contains all the parameters needed for two dimensional or three dimensional cure predictions. Current stereolithography process designs use the E_c–D_p model to translate a computer aided design (CAD) drawing into a bitmap of the exposure profile. By substituting the mechanistic model presented in this thesis in place of the existing E_c–D_p model, solid objects of various geometries can be generated from different cure recipes.

REFERENCES

[1] Anseth, K. and Bowman, C., "Kinetic gelation model predictions of crosslinked polymer network microstructure," *Chemical Engineering Science*, no. 14, pp. 2007–17, 1994.

[2] Berchtold, K. A., Lovestead, T. M., and Bowman, C. N., "Coupling chain length dependent and reaction diffusion controlled termination in the free radical polymerization of multivinyl (meth)acrylates," *Macromolecules*, vol. 35, no. 21, pp. 7968–7975, 2002.

[3] Bowman, C. N. and Peppas, N. A., "A kinetic gelation method for the simulation of free-radical polymerizations," *Chemical Engineering Science*, vol. 47, no. 6, pp. 1411–1419, 1992.

[4] Carothers, W. H., "Polymerization," *Chemical Reviews*, vol. 8, no. 3, pp. 353–426, 1931.

[5] Carothers, W. H., "Polymers and polyfunctionality," *Transactions of the Faraday Society*, vol. 32, no. 1, pp. 0039–0053, 1936.

[6] Decker, C. and Jenkins, A. D., "Kinetic approach of oxygen inhibition in ultraviolet-induced and laser-induced polymerizations," *Macromolecules*, vol. 18, no. 6, pp. 1241–1244, 1985.

[7] Flory, P. J., "Molecular size distribution in three dimensional polymers. i. gelation," *Journal of the American Chemical Society*, vol. 63, pp. 3083–3090, 1941.

[8] Gillespie, D. T., "Exact stochastic simulation of coupled chemical-reactions," *Abstracts of Papers of the American Chemical Society*, vol. 173, no. MAR20, pp. 128–128, 1977.

[9] Goodner, M. D. and Bowman, C. N., "Development of a comprehensive free radical photopolymerization model incorporating heat and mass transfer effects in thick films," *Chemical Engineering Science*, vol. 57, no. 5, pp. 887–900, 2002.

[10] Goodner, M. and Bowman, C., "Modeling and experimental investigation of light intensity and initiator effects on solvent-free photopolymerization," in *National Meeting of the American Chemical Society* (Long, T. and Hunt, M., eds.), vol. 713, (Las Vegas, Nevada), pp. 220–231, American Chemical Society, 1998.

[11] Gou, L. J., Coretsopoulos, C. N., and Scranton, A. B., "Measurement of the dissolved oxygen concentration in acrylate monomers with a novel photochemical method," *Journal of Polymer Science Part a-Polymer Chemistry*, vol. 42, no. 5, pp. 1285–1292, 2004.

[12] He, J. P., Zhang, H. D., and Yang, Y. L., "Monte-carlo simulation of chain-length distribution in radical polymerization with transfer-reaction," *Macromolecular Theory and Simulations*, vol. 4, no. 4, pp. 811–819, 1995.

[13] Hutchison, J. B. and Anseth, K. S., "Off-lattice approach to simulate radical chain polymerizations of tetrafunctional monomers," *Macromolecular Theory and Simulations*, vol. 10, no. 6, pp. 600–607, 2001.

[14] Hutchison, J. B. and Anseth, K. S., "Off-lattice simulation of multifunctional monomer polymerizations: Effects of monomer mobility, structure, and functionality on structural evolution at low conversion," *Journal of Physical Chemistry B*, vol. 108, no. 30, pp. 11097–11104, 2004.

[15] Krevelen, D. V., *Properties of Polymers*. Elsevier, 1976.

[16] Kurdikar, D. L. and Peppas, N. A., "A kinetic-study of diacrylate photopolymerizations," *Polymer*, vol. 35, no. 5, pp. 1004–1011, 1994.

[17] Lee, J. H., Prud'homme, R. K., and Aksay, I. A., "Cure depth in photopolymerization: Experiments and theory," *Journal of Materials Research*, vol. 16, no. 12, pp. 3536–3544, 2001.

[18] Lee, T. Y., Kaung, W., Jonsson, E. S., Lowery, K., Guymon, C. A., and Hoyle, C. E., "Synthesis and photopolymerization of novel multifunctional vinyl esters," *Journal of Polymer Science Part a-Polymer Chemistry*, vol. 42, no. 17, pp. 4424–4436, 2004.

[19] Lovestead, T. M., O'Brien, A. K., and Bowman, C. N., "Models of multivinyl free radical photopolymerization kinetics," *Journal of Photochemistry and Photobiology a-Chemistry*, vol. 159, no. 2, pp. 135–143, 2003.

[20] Manneville, P. and deSeze, L., *Percolation and Gelation by Additive Polymerization*. Numerical Methods in the Study of Critical Phenomena, Berlin: Springer-Verlag, 1981.

[21] Meimaroglou, D., Krallis, A., Saliakas, V., and Kiparissides, C., "Prediction of the bivariate molecular weight - long chain branching distribution in highly branched polymerization systems using monte carlo and sectional grid methods," *Macromolecules*, vol. 40, no. 6, pp. 2224–2234, 2007.

[22] Moad, G. and Solomon, D., "Termination," in *The Chemistry of Radical Polymerization*, pp. 233–278, Oxford: Elsevier, 2 ed., 2006.

[23] Nguyen, K. T. and West, J. L., "Photopolymerizable hydrogels for tissue engineering applications," *Biomaterials*, vol. 23, no. 22, pp. 4307–4314, 2002.

[24] O'Brien, A. K. and Bowman, C. N., "Impact of oxygen on photopolymerization kinetics and polymer structure," *Macromolecules*, vol. 39, no. 7, pp. 2501–2506, 2006.

[25] Odian, G., "Radical chain polymerization," in *Principles of Polymerization*, pp. 198–349, New York: John Wiley & Sons, 4 ed., 2004.

[26] Slopek, R., *In-Situ Monitoring of the Mechanical Properties During the Photopolymerization of Acrylate Resins Using Particle Tracking Microrheology*. PhD thesis, Georgia Institute of Technology, Atlanta, 2008.

[27] Tang, Y. Y., Henderson, C., Muzzy, J., and Rosen, D. W., "Stereolithography cure modelling and simulation," *International Journal of Materials & Product Technology*, vol. 21, no. 4, pp. 255–272, 2004.

[28] Tang, Y., *Stereolithography Cure Process Modeling*. PhD thesis, Georgia Institute of Technology, Atlanta, 2005.

[29] Unal, S., Oguz, C., Yilgor, E., Gallivan, M., Long, T. E., and Yilgor, I., "Understanding the structure development in hyperbranched polymers prepared by oligomeric a(2)+b-3 approach: comparison of experimental results and simulations," *Polymer*, vol. 46, no. 13, pp. 4533–4543, 2005.

[30] Wen, M., Scriven, L. E., and McCormick, A. V., "Kinetic gelation modeling: Structural inhomogeneity during cross-linking polymerization," *Macromolecules*, vol. 36, no. 11, pp. 4140–4150, 2003.

[31] Winter, H. H. and Chambon, F., "Analysis of linear viscoelasticity of a crosslinking polymer at the gel point," *Journal of Rheology*, vol. 30, no. 2, pp. 367–382, 1986.

[32] Zhang, X., Jiang, X. N., and Sun, C., "Micro-stereolithography of polymeric and ceramic microstructures," *Sensors and Actuators a-Physical*, vol. 77, no. 2, pp. 149–156, 1999.